

# Drastic magnetic-field-induced chiral current order and emergent current-bond-field interplay in kagome metal $AV_3Sb_5$ (A=Cs,Rb,K)

Rina Tazai<sup>1</sup>, Youichi Yamakawa<sup>2</sup>, and Hiroshi Kontani<sup>2</sup>

<sup>1</sup>*Yukawa Institute for Theoretical Physics, Kyoto University, Kyoto 606-8502, Japan*

<sup>2</sup>*Department of Physics, Nagoya University, Furo-cho, Nagoya 464-8602, Japan.*

(Dated: April 5, 2024)

In kagome metals, the chiral current order parameter  $\boldsymbol{\eta}$  with time-reversal-symmetry-breaking is the source of various exotic electronic states, while the method of controlling the current order and its interplay with the star-of-David bond order  $\boldsymbol{\phi}$  are still unsolved. Here, we reveal that tiny uniform orbital magnetization  $M_{\text{orb}}[\boldsymbol{\eta}, \boldsymbol{\phi}]$  is induced by the chiral current order, and its magnitude is prominently enlarged under the presence of the bond order. Importantly, we derive the magnetic-field ( $h_z$ )-induced Ginzburg-Landau (GL) free energy expression  $\Delta F[h_z, \boldsymbol{\eta}, \boldsymbol{\phi}] \propto -h_z M_{\text{orb}}[\boldsymbol{\eta}, \boldsymbol{\phi}]$ , which enables us to elucidate the field-induced current-bond phase transitions in kagome metals. The emergent current-bond- $h_z$  trilinear coupling term in the free energy,  $-3m_1 h_z \boldsymbol{\eta} \cdot \boldsymbol{\phi}$ , naturally explains the characteristic magnetic field sensitive electronic states in kagome metals, such as the field-induced current order and the strong interplay between the bond and current orders. The GL coefficients of  $\Delta F[h_z, \boldsymbol{\eta}, \boldsymbol{\phi}]$  derived from the realistic multiorbital model are appropriate to explain various experiments. Furthermore, we present a natural explanation for the drastic strain-induced increment of the current order transition temperature  $T_c$  reported by a recent experiment.

## Introduction

Recent discovery of unconventional quantum phases in metals has led to a new trend of condensed matter physics. Exotic charge-density-wave orders and unconventional superconductivity in geometrically frustrated kagome metal  $AV_3Sb_5$  (A=Cs,Rb,K) have been attracting increasing attention [1, 2]. The  $2 \times 2$  (inverse) star-of-David order, which is presumably the triple- $\boldsymbol{q}$  ( $3Q$ ) bond order (BO), occurs at  $T_{\text{BO}} \approx 100$  K at ambient pressure [3, 4]. The BO is the time-reversal-symmetry (TRS) preserving modulation in the hopping integral,  $\delta t_{ij}^b = \text{real}$ . [5–11]. Below  $T_{\text{BO}}$ , nodeless superconductivity occurs for A=Cs [12, 13], which is naturally explained based on the BO fluctuation mechanism proposed in Ref. [11].

In kagome metals, unusual TRS breaking (TRSB) phase without long-range spin orders has been reported by  $\mu$ -SR [14–17], Kerr rotation [18, 19], field-tuned chiral transport [20] measurements and STM studies under magnetic field [3, 20]. The transition temperature  $T_{\text{TRSB}}$  is still under debate. Although it is close to  $T_{\text{BO}}$  in many experiments, the TRSB order parameter is strongly magnified at  $T^* \approx 35$ K for A=Cs [14, 16, 20] and  $T^* \approx 50$ K for A=Rb [17]. Recently, magnetic torque measurement reveals the nematic order with TRSB at  $T^{**} \approx 130$ K [21], while no TRSB was reported by recent Kerr rotation study [22]. A natural candidate is the correlation driven TRSB hopping integral modulation:  $\delta t_{ij}^c = \text{imaginary}$ . This order accompanies topological charge-current [23] that gives the giant anomalous Hall effect (AHE) [24, 25].

Theoretically, the BO and the current order emerge

in the presence of sizable off-site electron correlations in Fe-based and cuprate superconductors [26–34] and in kagome metals [7–9, 11, 35–39]. Notably, strong off-site interaction (due to the off-site Coulomb repulsion or the BO fluctuations) gives rise to the charge current order [8–10, 35]. Based on the GL free-energy analysis, interesting bond+current nematic ( $C_2$ ) coexisting phases have been discussed in two-dimensional (2D) and three-dimensional (3D) models [9, 35, 37–39]. Experimentally, the nematic state is actually observed by the elastoresistance [40], the scanning birefringence [18], and the STM [4] measurements.

In kagome metals, outer magnetic field  $h_z$  drastically modifies the electronic states. The chirality of the charge-current is aligned under very tiny  $|h_z| \sim 1$  Tesla according to the measurements of AHE [24, 25] and field-tuned chiral transport [20]. In addition, the amplitude of the loop current is strongly magnified by applying small  $h_z$  ( $\gtrsim 1$  Tesla) [15–17]. Very recent transport measurement of highly symmetric fabricated  $CsV_3Sb_5$  micro sample [41] reveals that current-order state is drastically enlarged by the small  $h_z$ . These drastic  $h_z$ -dependences are the hallmarks of the TRSB state, and it is important to understand the coupling between the current order, chirality and the magnetic field in kagome metals.

In this paper, we reveal that the  $3Q$  loop-current order parameters accompany tiny orbital magnetization,  $M_{\text{orb}}$ , and its magnitude is drastically enlarged under the presence of the bond order. Importantly, we derive the  $h_z$ -induced Ginzburg-Landau (GL) free energy expression  $\Delta F$ , which is useful to study nontrivial phase transitions under the magnetic field. The emergent current-bond- $h_z$  trilinear coupling term in  $\Delta F$  not only explains the origin of novel field-induced chiral symmetry breaking [15–17] but also provides useful hints to control the charge cur-

\*These authors made equal contribution to the work.

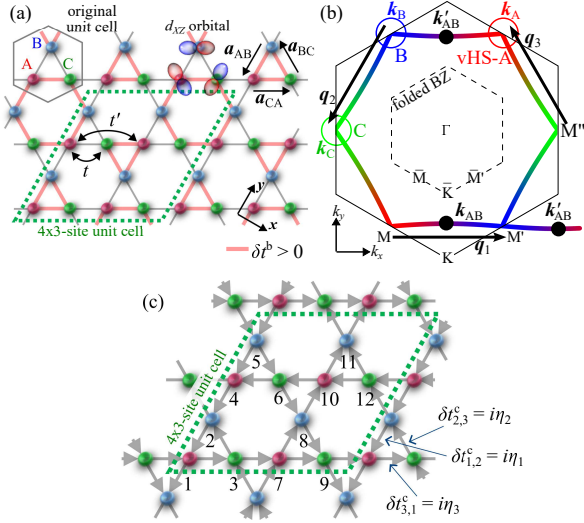


FIG. 1: (a) Kagome lattice tight-binding model. The  $3Q$  BO  $\phi = (\phi, \phi, \phi)/\sqrt{3}$  ( $\phi > 0$ ) is depicted. The  $d_{XZ}$ -orbital on each sublattice is drawn. (b) FS at the vHS filling  $n_{\text{vHS}}$ . Three vHS points  $\mathbf{k}_A$ ,  $\mathbf{k}_B$  and  $\mathbf{k}_C$  are respectively composed of  $A$  (red),  $B$  (blue), and  $C$  (green) orbitals. The inter-vHS nesting vectors  $\mathbf{q}_n$  ( $n = 1 - 3$ ) are shown. (c)  $3Q$  current order  $\boldsymbol{\eta} = (\eta_1, \eta_2, \eta_3)$  is depicted. Note that  $(\eta_1, \eta_2, \eta_3)$  and  $(\eta_1, -\eta_2, -\eta_3)$  are the same bulk states.

rent in kagome metals. In addition, the “strain-induced increment of  $T_{\text{TRSB}}$  reported in Ref. [41] is naturally understood.

In the present study of  $M_{\text{orb}}$ , we mainly focus on the current order in the  $3d_{XZ}$ -orbital (in  $b_{3g}$ -representation) of V ion, which has been intensively studied previously [7–10, 35]. However, other  $3d$ -orbitals (especially  $3d_{YZ}$ ,  $d_{X^2-Y^2}$ ,  $d_{3Z^2-R^2}$ -orbitals) also form the large Fermi surfaces (FSs) with the van-Hove singularity (vHS) points near the Fermi level. The impact of these non- $b_{3g}$  orbitals on the current order has also been studied in Refs. [37, 39]. The present field-induced GL theory does not depend on the  $d$ -orbital character of the current order parameter. We calculate the GL coefficients  $m_n$  ( $n = 1 - 3$ ) for various  $d$ -orbital current order states based on the first-principles kagome metal models. For a fixed order parameter,  $m_n$  is large when the FS reconstruction due to the current order parameters occurs near the vHS points.

### Model Hamiltonian with current and bond orders

Here, we study the kagome-lattice tight-binding model with  $b_{3g}$  (or  $d_{XZ}$ ) orbitals shown in Fig. 1 (a). Each unit-cell is composed of three sublattices  $A$ ,  $B$ ,  $C$ . We set the nearest-neighbor hopping integral  $t = -0.5[\text{eV}]$ . In addition, we introduce the nearest intra-sublattice hopping  $t' = -0.02[\text{eV}]$  shown in Fig. 1 (a) to avoid the perfect nesting. (Hereafter, the unit of the energy is eV.) The FS at the vHS filling,  $n = n_{\text{vHS}} = 2.55$  per 3-site unit cell,

is shown in Fig. 1 (b). Then, the FS lies on the three vHS points ( $\mathbf{k}_A$ ,  $\mathbf{k}_B$ ,  $\mathbf{k}_C$ ), each of which is composed of a single sublattice  $A$ ,  $B$ , or  $C$ . This simple three-orbital model well captures the main pure-type FS in kagome metals [3, 42–45].

The bond/current order is the modulation of the hopping integral between  $i$  and  $j$  atoms due to the electron correlation,  $\delta t_{ij}^{b/c}$ . Theoretically, it is the symmetry breaking in the self-energy, and it is derived from the density-wave (DW) equation [11, 35]. The wavevectors of the bond and current orders correspond to the inter-sublattice nesting vectors  $\mathbf{q}_n$  ( $n = 1 - 3$ ) in Fig. 1 (b) according to previous theoretical studies [7–9, 11, 35, 36]. The triple  $Q$  ( $3Q$ ) current order between the nearest atoms is depicted in Fig. 1 (c). The form factor (=normalized  $\delta t_{ij}^c$ ) with  $\mathbf{q} = \mathbf{q}_1$ ,  $f_{ij}^{(1)}$ , is  $+i$  for  $(i, j)$  belongs to the sites  $(l, m) = (1, 2), (2, 4), (4, 5), (5, 1)$  in Fig. 1 (c), and  $-i$  for  $(7, 8), (8, 10), (10, 11), (11, 7)$ . Odd parity relation  $f_{ij}^{(1)} = -f_{ji}^{(1)}$  holds. Other form factors with  $\mathbf{q}_2$  and  $\mathbf{q}_3$ ,  $f_{ij}^{(2)}$  and  $f_{ij}^{(3)}$ , are also derived from Fig. 1 (c). Using  $\mathbf{f}_{ij} = (f_{ij}^{(1)}, f_{ij}^{(2)}, f_{ij}^{(3)})$ , the current order is

$$\delta t_{ij}^c = \boldsymbol{\eta} \cdot \mathbf{f}_{ij}, \quad (1)$$

where  $\boldsymbol{\eta} \equiv (\eta_1, \eta_2, \eta_3)$  is the set of current order parameters with the wavevector  $\mathbf{q}_m$ . Also, the BO is given as

$$\delta t_{ij}^b = \boldsymbol{\phi} \cdot \mathbf{g}_{ij}, \quad (2)$$

where  $\boldsymbol{\phi} \equiv (\phi_1, \phi_2, \phi_3)$  is the set of BO parameters with the wavevector  $\mathbf{q}_m$ , and  $g_{ij}^{(m)} = g_{ji}^{(m)} = \pm 1$  is the even-parity form factor for the BO shown in Fig. 1 (a). For example,  $g_{ij}^{(1)} = +1$  [ $-1$ ] for  $(i, j)$  belongs to  $(1, 2), (4, 5), (8, 10), (11, 7)$  [ $(2, 4), (5, 1), (7, 8), (10, 11)$ ].

The unit cell under the  $3Q$  bond/current order is magnified by  $2 \times 2$  times. Thus, we analyze the electronic states with the current order based on the  $4 \times 3$ -site kagome lattice model. The Hamiltonian with the bond+current order is  $\hat{H} = \sum_{\mathbf{k}, l, m, \sigma} h_{lm}(\mathbf{k}) c_{\mathbf{k}, l, \sigma}^\dagger c_{\mathbf{k}, m, \sigma}$ , where  $l, m = 1 \sim 12$  and  $h_{lm}(\mathbf{k}) (= h_{ml}(\mathbf{k})^*)$  is the Fourier transform of the hopping integral  $\tilde{t}_{ij} = t_{ij} + \delta t_{ij}^b + \delta t_{ij}^c$ . Here,  $t_{ij}$  is the hopping integral of the original model, and  $\delta t_{ij}^{b(c)}$  is the hopping integral due to the bond (current) order in Eq. [2] (Eq. [1]).

### Uniform orbital magnetization

The TRS is broken in the presence of the current order  $\delta t_{ij}^c$ . In this case, the uniform orbital magnetization  $M_{\text{orb}}$  may appear due to the finite Berry curvature as pointed out in Ref. [9].  $M_{\text{orb}}$  per V atom in the unit of Bohr magneton  $\mu_B = e\hbar/2m_e c$  ( $m_e =$  free electron mass) is given as [46, 47]

$$M_{\text{orb}} = \frac{\mu_B}{E_0 N_{\text{uc}} N} \sum_{\mathbf{k}, \sigma} m(\mathbf{k}), \quad (3)$$

$$m(\mathbf{k}) = \sum_{\alpha \neq \beta} \text{Im}(V_{\beta\alpha\mathbf{k}}^* \times V_{\beta\alpha\mathbf{k}})_z$$

$$\times \left( (\epsilon_{\beta\mathbf{k}} - \epsilon_{\alpha\mathbf{k}})n(\epsilon_{\alpha\mathbf{k}}) - 2T \ln[1 + e^{-(\epsilon_{\alpha\mathbf{k}} - \mu)/T}] \right), \quad (4)$$

$$V_{\alpha\beta\mathbf{k}} = \langle \alpha\mathbf{k} | \nabla_{\mathbf{k}} h_{\mathbf{k}} | \beta\mathbf{k} \rangle / (\epsilon_{\alpha\mathbf{k}} - \epsilon_{\beta\mathbf{k}}), \quad (5)$$

where  $\epsilon_{\alpha\mathbf{k}}$  is  $\alpha$ -th eigenenergy of  $4 \times 3$ -site kagome lattice model in the folded BZ.  $n(\epsilon)$  is Fermi distribution function,  $N_{\text{uc}} = 12$  is the site number of  $2 \times 2$  unit cell,  $N$  is the  $\mathbf{k}$ -mesh number, and  $E_0 = \hbar^2/a^2 m_e$ .  $a$  is the unit length in the numerical study, and we set  $a = |\mathbf{a}_{\text{AB}}|$  ( $= 0.275$  nm in kagome metals).  $E_0 = 1.0$  eV when  $a = 0.275$  nm.

At zero temperature, Eq. [3] is rewritten as

$$M_{\text{orb}}^{T=0} = \frac{\mu_{\text{B}}}{E_0 N_{\text{uc}} N} \sum_{\mathbf{k}, \alpha < \beta} \text{Im}\{V_{\beta\alpha\mathbf{k}}^x V_{\alpha\beta\mathbf{k}}^y - (\alpha \leftrightarrow \beta)\}$$

$$\times (\epsilon_{\alpha\mathbf{k}} + \epsilon_{\beta\mathbf{k}} - 2\mu)(n^0(\epsilon_{\alpha\mathbf{k}}) - n^0(\epsilon_{\beta\mathbf{k}})), \quad (6)$$

where  $n^0(\epsilon)$  is the Fermi distribution function at  $T = 0$ . Considering the factor  $(n^0(\epsilon_{\alpha\mathbf{k}}) - n^0(\epsilon_{\beta\mathbf{k}}))$  with  $\alpha < \beta$ ,  $M_{\text{orb}}$  originates from the ‘‘vertical particle-hole (p-h) excitation’’, from  $\epsilon_{\alpha\mathbf{k}} < 0$  to  $\epsilon_{\beta\mathbf{k}} > 0$ , at the same  $\mathbf{k}$  in the folded BZ.

The folded FS ( $\eta = \phi = 0$ ) and bandstructure in the folded Brillouin zone (BZ) at  $n = n_{\text{vHS}}$  are shown in Figs. S1 (a)-(c) in the SI A [49]. Here, all vHS points A, B, C in the original BZ in Fig. 1 (b) move to  $\Gamma$  point, and they will hybridize each other due to the current and/or BO parameter. When  $n \approx n_{\text{vHS}}$ , prominent band hybridization occurs near the  $\Gamma$  point, as understood in Fig. S1 (a). Then, the bonding (antibonding) band energy at  $\Gamma$  point is below (above) the Fermi level, as shown in Fig. S1 (b). Because of the factor  $\text{Im}\{\dots\} \propto |\epsilon_{\alpha\mathbf{k}} - \epsilon_{\beta\mathbf{k}}|^{-2}$  in Eq. [6],  $M_{\text{orb}}$  becomes large when  $n \approx n_{\text{vHS}}$ .

Here, we calculate  $M_{\text{orb}}$  [ $\mu_{\text{B}}$ ] near the vHS filling  $n_{\text{vHS}} = 2.55$  at  $T = 1$  meV, in the case of  $E_0 = 1.0$  eV. Figure 2 (a) represents the obtained  $M_{\text{orb}}$  under the 3Q current order  $\boldsymbol{\eta} = (\eta, \eta, \eta)/\sqrt{3}$  for  $n = 2.47 \sim 2.63$ . (The FS without the current order is shown in Fig. 2 (b).) We obtain the relation  $M_{\text{orb}} \propto \eta^3$ , and it becomes large when the filling is close to  $n_{\text{vHS}}$ . Therefore, the 3Q current order state is a weak-ferromagnetic (or ferrimagnetic) state. Because the additional free energy under the magnetic field  $h_z$  per 3-site unit cell is

$$\Delta F = -3h_z M_{\text{orb}}, \quad (7)$$

the chirality of the current order is aligned under tiny  $h_z$ . In other words, the 3Q current order is stabilized under  $h_z$ . In contrast,  $M_{\text{orb}} = 0$  for 1Q and 2Q current orders.  $h_z = 10^{-4}$  corresponds to  $\sim 1$  Tesla.

Here, we present a symmetry argument to understand  $M_{\text{orb}}$  induced by the current order. Both 1Q and 2Q current orders are invariant under the time-reversal and the translational operations successively. Therefore,  $M_{\text{orb}} = 0$  due to the TRS in the bulk state. In contrast,

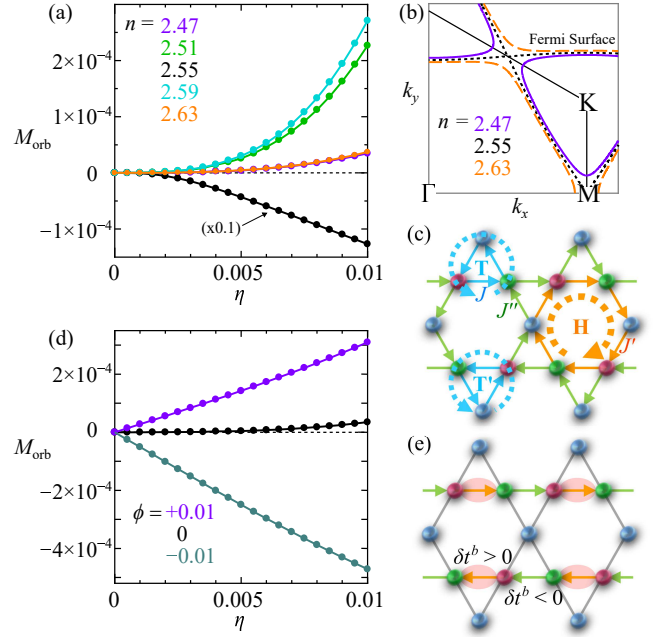


FIG. 2: (a)  $M_{\text{orb}}$  [ $\mu_{\text{B}}$ ] per V atom due to the 3Q current order  $\boldsymbol{\eta} = (\eta, \eta, \eta)/\sqrt{3}$  at  $T = 1$  meV for  $n = 2.47 \sim 2.63$ .  $M_{\text{orb}} (\propto \eta^3)$  is large when  $n \approx n_{\text{vHS}}$ . (b) FS around  $n_{\text{vHS}} = 2.55$ . (c) Charge-current pattern in real space.  $J \neq J' \neq J''$  in spite of the same order parameter  $\eta_1 = \eta_2 = \eta_3$ . (d)  $M_{\text{orb}} (\propto \eta)$  due to the coexistence of 3Q current order and 3Q BO at  $n = 2.47$ . (e) 1Q bond+current order with finite  $M_{\text{orb}}$ . Its time-reversal and translation by  $2\mathbf{a}_{\text{AB}}$  causes a different state.

$M_{\text{orb}}$  is nonzero in the 3Q current order because this state breaks the TRS in the bulk state [9]. To find an intuitive reason, we calculated the charge-current along the nearest bonds  $J_{ij}$  in the 3Q state using the method in Refs. [33, 48], and found that  $|J_{ij}|$  is bond-dependent in spite of the same order parameter  $\eta_1 = \eta_2 = \eta_3$ . The obtained relation  $J \neq J' \neq J''$  shown in Fig. 2 (c) indicates that  $M_{\text{orb}}$  becomes finite because the magnetic fluxes through triangles and hexagons do not cancel perfectly.

For general order parameter  $\boldsymbol{\eta} = (\eta_1, \eta_2, \eta_3)$ , we verified the relation  $M_{\text{orb}} \propto \eta_1 \eta_2 \eta_3$  up to the third-order. In fact, based on the perturbation theory with respect to Eq. [1];  $\eta_m \hat{f}^{(m)}$  ( $m = 1 - 3$ ).  $M_{\text{orb}}[\boldsymbol{\eta}]$  is expanded as  $\sum_{pqr} b_{pqr} (\eta_1)^p (\eta_2)^q (\eta_3)^r$  with  $p + q + r = \text{odd}$  because  $M_{\text{orb}}[\boldsymbol{\eta}]$  is an odd function of  $\boldsymbol{\eta}$ . In addition,  $b_{pqr}$  can be nonzero only when  $p\mathbf{q}_1 + q\mathbf{q}_2 + r\mathbf{q}_3 = \mathbf{0}$  (modulo original reciprocal vectors), because we study the nonlinear response of the uniform ( $\mathbf{q} = \mathbf{0}$ ) magnetization due to the potential  $\eta_m f^{(m)}$  with wavevector  $\mathbf{q}_m$  in the original unit cell. (See the SI B for a more detailed explanation [49].) In Fig. 2 (a),  $M_{\text{orb}}$  originates from the third-order term  $b_{111}$ , which is allowed because of the momentum conservation  $\mathbf{q}_1 + \mathbf{q}_2 + \mathbf{q}_3 = \mathbf{0}$ .

Next stage, we calculate  $M_{\text{orb}}$  under the coexistence of the 3Q current order  $\boldsymbol{\eta} = (\eta, \eta, \eta)/\sqrt{3}$  and the 3Q bond order  $\boldsymbol{\phi} = (\phi, \phi, \phi)/\sqrt{3}$ . Figure 2 (d) represents  $M_{\text{orb}}$

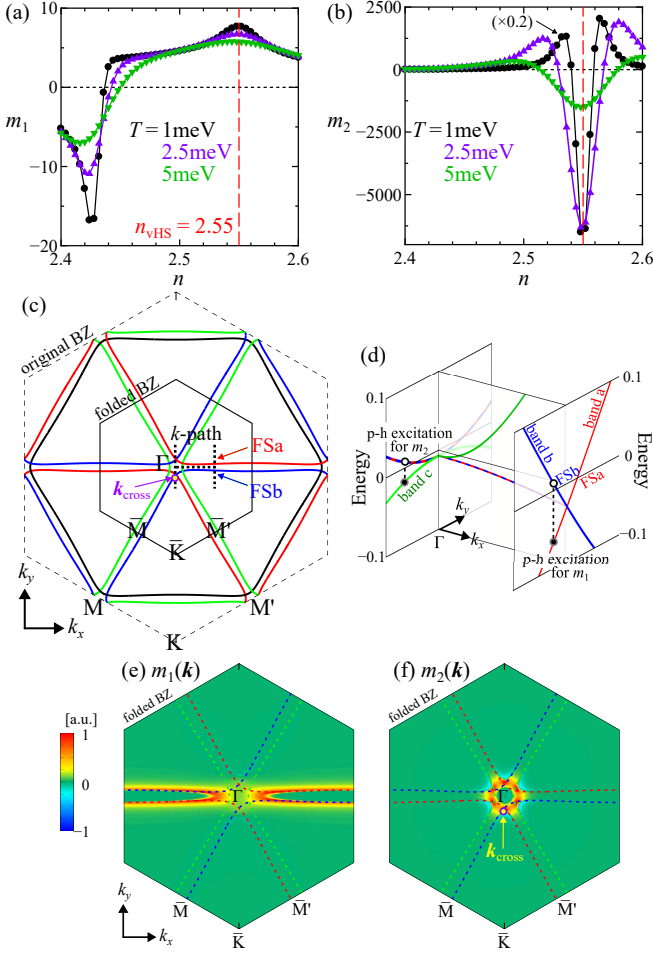


FIG. 3: Obtained coefficients of  $\bar{M}_{\text{orb}}$ , (a)  $m_1$  and (b)  $m_2$  ( $\approx -m_3$ ), per  $V$  atom as a function of  $n$ . Both  $|m_1|$  and  $|m_2|$  are large for  $n \sim n_{\text{vHS}}$ . (c) Folded FS and (d) folded bandstructure in the folded BZ when  $\boldsymbol{\eta} = \boldsymbol{\phi} \rightarrow \mathbf{0}$ . The  $\mathbf{k}$ -path is shown in the (c). We set the origin of the energy at the vHS energy. (e)  $m_1(\mathbf{k}) \equiv \partial^2 m(\mathbf{k}) / \partial \eta_1 \partial \phi_1 |_{\eta=\phi=0}$  and (f)  $m_2(\mathbf{k}) \equiv \partial^3 m(\mathbf{k}) / \partial \eta_1 \partial \eta_2 \partial \eta_3 |_{\eta=\phi=0}$  for  $n = 2.58$  ( $n_{\text{vHS}} = 2.55$ ). Note that  $m_n \propto \sum_{\mathbf{k}} m_n(\mathbf{k})$ .

at  $\phi = 0, \pm 0.01$  as a function of  $\eta$ , for  $n = 2.47$  and  $T = 1$  meV. Interesting relation  $M_{\text{orb}} \propto \eta$  is obtained when  $\phi \neq 0$ . Then, the field-induced  $\Delta F$  contains a non-analytic  $\eta$ -linear term that always produces  $\langle \eta \rangle \neq 0$ . This fact causes significant field-induced change in the phase diagram, as we will explain in the SI C [49].

To understand the  $\eta$ -linear term in Fig. 2 (d), we expand  $M_{\text{orb}}$  with respect to the current order  $\eta_m \hat{f}^{(m)}$  and bond order  $\phi_m \hat{g}^{(m)}$ . Its Taylor expansion is  $\sum_{pqr p'q'r'} b_{pqr}^{p'q'r'} (\eta_1)^p (\eta_2)^q (\eta_3)^r (\phi_1)^{p'} (\phi_2)^{q'} (\phi_3)^{r'}$  with  $p+q+r = \text{odd}$  and  $(p+p')\mathbf{q}_1 + (q+q')\mathbf{q}_2 + (r+r')\mathbf{q}_3 = \mathbf{0}$  (modulo original reciprocal vectors). The  $\eta$ -linear term in Fig. 2 (c) mainly originates from the second-order term  $b_{100}^{100}$  in addition to the third-order term  $b_{100}^{011}$ . In fact, the  $1Q$  current +  $1Q$  BO state shown in Fig. 2 (e) violates the TRS in the bulk state.

## Field-induced GL free energy expression

From the above discussions, we obtain the following convenient expression of the orbital magnetization and the “field-induced GL free energy formula” up to the third-order:

$$\begin{aligned} \bar{M}_{\text{orb}} &= m_1 \boldsymbol{\phi} \cdot \boldsymbol{\eta} + m_2 \eta_1 \eta_2 \eta_3 \\ &\quad + m_3 (\eta_1 \phi_2 \phi_3 + \phi_1 \eta_2 \phi_3 + \phi_1 \phi_2 \eta_3), \quad (8) \\ \Delta \bar{F} &= -3h_z \bar{M}_{\text{orb}}, \quad (9) \end{aligned}$$

which enables us to elucidate the field-induced bond+current phase transitions in kagome metals. Figures 3 (a) and (b) show the coefficients  $m_1$  and  $m_2$  derived from Eq. [3] numerically, respectively. Interestingly,  $|m_1|$  and  $|m_2|$  become large for  $n \sim n_{\text{vHS}}$ .

In the SI D [49], we show that  $\bar{M}_{\text{orb}}$  in Eq. [8] well reproduces the original  $M_{\text{orb}}$  when  $|\boldsymbol{\eta}|, |\boldsymbol{\phi}| \lesssim 0.02$ . The expression of  $\bar{M}_{\text{orb}}$  is also justified based on the first principles model for  $|\boldsymbol{\eta}|, |\boldsymbol{\phi}| \lesssim 0.02$  in the SI D [49].

To understand the  $n$ -dependences of  $m_1$  and  $m_2$ , we discuss the folded FS and bandstructure given in Figs. 3 (c) and (d), respectively, for  $\boldsymbol{\eta} = \boldsymbol{\phi} \rightarrow \mathbf{0}$ . Here, band  $a$  [b, and c] originates from the bandstructure around vHS-A [B,C] in Fig. 1 (b). As shown in Fig. 3 (d), band  $a$  and band  $b$  degenerate along  $k_x$ -axis and  $k_y$ -axis. Hereafter, we set  $\mu = 0$ .

First, we consider the origin of  $m_1$ , which is caused by the band-folding induced by  $\eta_1 \hat{f}^{(1)}$  and  $\phi_1 \hat{g}^{(1)}$ , both of which convey the wavevector  $\mathbf{q} = \mathbf{q}_1$ . Therefore,  $m_1$  is induced by the “vertical p-h excitation between band  $a$  and band  $b$ ” in Fig. 3 (d) in the folded BZ. (Band  $c$  gives no contribution for  $m_1$ .) To verify this consideration, we examine the function  $m(\mathbf{k})$  in Eq. [4]. Figure 1 (e) shows the obtained  $m_1(\mathbf{k}) \equiv \partial^2 m(\mathbf{k}) / \partial \eta_1 \partial \phi_1 |_{\eta=\phi=0}$ . (Note that  $m_1 \propto \sum_{\mathbf{k}} m_1(\mathbf{k})$ .) It is verified that large  $m_1$  originates from the FS  $a$  and FS  $b$  near the  $\Gamma$ -M line in Fig. 3 (c). This mechanism occurs for both  $n > n_{\text{vHS}}$  and  $n < n_{\text{vHS}}$ , so  $|m_1|$  takes large value for a wide range of  $n$ . Note that  $m_1$  in Fig. 3 (a) changes its sign at  $n = 2.44$ , when  $\mathbf{k}_{\text{AB}}$  and  $\mathbf{k}'_{\text{AB}}$  in Fig.1 (b) touch in the folded BZ.

Next, we consider the origin of  $m_2$ , which is caused by the band-foldings caused by  $\hat{f}^{(1)}$  (at  $\mathbf{q} = \mathbf{q}_1$ ),  $\hat{f}^{(2)}$  (at  $\mathbf{q} = \mathbf{q}_2$ ) and  $\hat{f}^{(3)}$  (at  $\mathbf{q} = \mathbf{q}_3$ ). This situation allows the “vertical p-h excitation between band  $a + b$  and band  $c$ ” in Fig. 3 (d), which is significant because the band splitting between  $\epsilon_{c\mathbf{k}}$  ( $> 0$ ) and  $\epsilon_{a,b\mathbf{k}}$  ( $< 0$ ) is very small. This process gives huge  $|m_2|$  at  $n = n_{\text{vHS}}$  obtained in Fig. 3 (b). Figure 3 (f) shows the obtained  $m_2(\mathbf{k}) \equiv \partial^3 m(\mathbf{k}) / \partial \eta_1 \partial \eta_2 \partial \eta_3 |_{\eta=\phi=0}$ . (Note that  $m_2 \propto \sum_{\mathbf{k}} m_2(\mathbf{k})$ .) The large  $m_2$  originates from the six band-crossing points ( $\mathbf{k}_{\text{cross}}$ ) near the  $\Gamma$  point, due to the vertical p-h excitation among three bands  $a, b, c$ .

To summarize, large  $|m_1|$  and  $|m_2|$  are caused by the FS crossing near the vHS points and the M-M' line for

$n \sim n_{\text{vHS}}$ . Therefore, the field-induced free energy  $\Delta\bar{F}$  should be significant in real kagome metals. In the SI B [49], we verify that the relation  $m_3 \approx -m_2$  holds very well. This relation originates from the relation  $f_{ij}^{(m)} = ig_{ij}^{(m)}$  or  $-ig_{ij}^{(m)}$  when both order parameters are composed of only the nearest bonds.

We verified in the SI E [49] that the magnitudes of  $m_1$  and  $m_2$  at  $t' = -0.08$  is comparable to those in Fig. 3. When  $t' = -0.02$  in Fig. 3 (b), the obtained  $m_2(n_{\text{vHS}})$  takes a large value because the p-h asymmetry around  $E = E_{\text{vHS}}$  is significant. When  $t' = -0.08$  in Fig. S6 (e), in contrast,  $m_2(n_{\text{vHS}})$  is small and  $m_2(n)$  tends to be an odd function of  $n - n_{\text{vHS}}$  because of the approximate p-h symmetry and the factor  $(\epsilon_{\alpha\mathbf{k}} + \epsilon_{\beta\mathbf{k}} - 2\mu)$  in Eq. [6]. (The numerical results of  $m_2(n)$  in the 30-orbital model in Figs. 5 (g)-(h) are closer to the results at  $t' = -0.02$  near the vHS filling.)

Below, we derive the order parameters under  $h_z$  by minimizing the GL free energy  $F = F^0 + \Delta\bar{F}$ , where  $F^0 = F_\eta^0 + F_\phi^0 + F_{\eta,\phi}^0$  is the free energy at  $h_z = 0$  [9, 35]:

$$\begin{aligned} F_\phi^0 &= a_b|\phi|^2 + b_1\phi_1\phi_2\phi_3 \\ &\quad + d_1(\phi_1^4 + \phi_2^4 + \phi_3^4) + d_2(\phi_1^2\phi_2^2 + (\text{cycl.})), \quad (10) \\ F_\eta^0 &= a_c|\eta|^2 + d_3(\eta_1^4 + \eta_2^4 + \eta_3^4) + d_4(\eta_1^2\eta_2^2 + (\text{cycl.})) \quad (11) \end{aligned}$$

and  $F_{\eta,\phi}^0$  contains the current-bond cross terms proportional to  $\eta^2\phi^1$  and  $\eta^2\phi^2$ :

$$\begin{aligned} F_{\eta,\phi}^0 &= b_2(\phi_1\eta_2\eta_3 + (\text{cycl.})) \\ &\quad + 2d_5(\phi_1^2\eta_1^2 + \phi_2^2\eta_2^2 + \phi_3^2\eta_3^2) + d_6(\phi_1^2\eta_2^2 + (\text{cycl.})) \quad (12) \end{aligned}$$

Here,  $a_{c(b)} = r_{c(b)}(T - T_{c(b)}^0)$ , where  $T_{c(b)}^0$  is the current-order (BO) transition temperature without other orders. Theoretically,  $a_{c(b)} \sim N(0)(-1 + \lambda_{\eta(\phi)}^{-1})$ , where  $N(0)$  is the density-of-states ( $\sim 1 \text{ eV}^{-1}$ ) and  $\lambda_{\eta(\phi)}$  is the DW equation eigenvalue of the current order (bond order) [50].  $\lambda_{\eta(\phi)} = 1$  at  $T = T_{c(b)}^0$ , while  $\lambda_{\eta(\phi)} = 0$  (*i.e.*,  $a_{c(b)} = \infty$ ) in the absence of interaction. According to Ref. [50],  $r_b T_b^0 \sim 0.1N(0)$  for the nematic BO in FeSe, while the corresponding value for BCS superconductors is  $\sim N(0)$ .

To discuss the phase diagram qualitatively, we set  $m_1 = 5$ ,  $m_2 = -m_3 = -1000$ , both of which are moderate compared with the values in Fig. 3. We also put  $d_i = 150$  ( $i = 1 - 4$ ) by seeing the numerical results in the SI F [49] and set  $r_c = r_b = 30$ . Then, both current and bond orders become  $3Q$  states because of the relations  $2d_1/d_2 > 1$  and  $2d_3/d_4 > 1$ . A more detailed explanation for the GL parameters is presented in the SI F [49].

### $h_z$ -effect on $3Q$ current order state

In this section, we demonstrate that the  $3Q$  current order state is drastically modified by  $h_z$ . Figure 4 (a)

shows the obtained  $3Q$  current order  $\boldsymbol{\eta} = (\eta_1, \eta_2, \eta_3)$  with  $\eta_1 = \eta_2 = \eta_3$ , when  $T_c^0 = 0.01$  in the absence of BO ( $T_b^0 = -\infty$ ). Here, we set  $h_z = 0 \sim 2 \times 10^{-3}$ . Because of the  $\eta^3$ -term by  $m_2 = -1000$ ,  $3Q$  current order  $\boldsymbol{\eta} = (\eta, \eta, \eta)/\sqrt{3}$  with negative  $\eta$  is stabilized in the presence of  $h_z > 0$ . In addition, the field-induced first-order transition occurs at  $T = T_c^0 + \Delta T_c$ , where  $\Delta T_c = (h_z m_2)^2/4r_c(d_3 + d_4)$  is quite small.

Next, we demonstrate the  $h_z$ -induced  $3Q$  current order state above  $T_c^0$  inside the BO state. Under the  $3Q$  BO phase  $\boldsymbol{\phi} = (\phi, \phi, \phi)/\sqrt{3}$ , the 2nd order GL coefficient  $a_c$  in Eq. [11] is renormalized as  $\bar{a}_c = a_c + (d_5 + d_6)(2\phi^2/3)$  due to the  $d_5, d_6$  terms. It is given as  $\bar{a}_c = \bar{r}_c(T - \bar{T}_c^0)$ , where  $\bar{T}_c^0 < T_c^0$  and  $\bar{r}_c < r_c$  as we explain in the SI F [49]. The smallness of  $\bar{r}_c$  is favorable for the  $h_z$ -induced current order. In this subsection, we simply denote  $\bar{T}_c^0$  and  $\bar{r}_c$  as  $T_c^0$  and  $r_c$ , respectively.

First, we drop the 3rd order GL terms  $b_i$  ( $i = 1, 2$ ) to concentrate on the field-induced novel phenomena. Figure 4 (b) exhibits the  $3Q$  current order with  $T_c^0 = 0.005$ , in the presence of the BO phase below  $T_b^0 = 0.01$ . For  $h_z = 1 \times 10^{-4}$  and  $2 \times 10^{-4}$ ,  $\eta$  starts to emerge just below  $T_b^0$  thanks to the  $\eta$ -linear term  $\Delta\bar{F} = -3h_z(m_1\phi + m_3\phi^2)\eta$ , and therefore  $T_c = T_b^0$ . When  $h_z \neq 0$ ,  $T_c^0$  is just a crossover temperature. To understand the role of the non-analytic term qualitatively, we analyze a simple GL free energy with a  $\eta$ -linear term in the SI C [49]: It is found that the field-induced current order  $|\boldsymbol{\eta}_{\text{ind}}|$  under the BO  $\boldsymbol{\phi}$  is approximately given as

$$|\boldsymbol{\eta}_{\text{ind}}| \approx 9|m_1 h_z \phi|/2a_c. \quad (13)$$

Thus, the field-induced  $|\boldsymbol{\eta}_{\text{ind}}|$  is prominent when the system at  $h_z = 0$  is close to the current order state (*i.e.*,  $a_c \gtrsim 0$ ). The expression of  $|\boldsymbol{\eta}_{\text{ind}}|$  in Eq. [13] is proportional to  $\boldsymbol{\phi}$  in contrast to Eq. (31) of Ref. [9].

A schematic picture for the field-induced current order is shown in Fig. 4 (c). In the  $3Q$  BO phase  $\boldsymbol{\phi} \propto (1, 1, 1)$ , the field-induced  $\boldsymbol{\eta}$  above  $T_c^0$  is proportional to  $\boldsymbol{\phi}$  to maximize  $\bar{M}_{\text{orb}} \propto \boldsymbol{\phi} \cdot \boldsymbol{\eta}$ . This coexisting state ( $\boldsymbol{\eta} \propto \boldsymbol{\phi}$ ) has  $C_6$  symmetry; see Ref. [35].

Next, we consider the effect of 3rd order GL terms in Fig. 4 (d), by setting  $-b_1 = b_2 = 1.0$ . (The relation  $b_1 b_2 < 0$  is general [35].) Due to the energy gain from the  $b_1$ -term,  $3Q$  BO  $\boldsymbol{\phi} \propto (1, 1, 1)$  appears at  $T \approx T_b^0 = 0.01$  as the first order transition [9]. At  $h_z = 0$ , the  $3Q$  current order  $\boldsymbol{\eta} = (\eta, \eta, -\eta')$  appears below  $T_c^0 = 0.005$  to maximize the energy gain from the  $b_2$  term ( $b_1 b_2 < 0$ ), as explained in Ref. [35]. Just below  $T_c^0$  ( $|\phi| \gg |\eta|$ ),  $\eta' = 2\eta$  is satisfied. (More generally,  $\boldsymbol{\eta} \propto (\eta_1, \eta_2, -\eta_1 - \eta_2)$ .) Figure 4 (e) depicts the ‘‘nematic’’ bond+current coexisting state below  $T_c^0$  with  $\boldsymbol{\eta} \sim (1, 1, -1)$  and  $\boldsymbol{\phi} \sim (1, 1, 1)$ ; see Ref. [35] for detail.

For  $h_z = 4 \times 10^{-4}$  in Fig. 4 (d), the field-induced  $3Q$  current order  $\boldsymbol{\eta} \propto (1, 1, 1)$  start to emerge just below  $T_b^0$ , similarly to Fig. 4 (b). The realized  $C_6$  symmetry

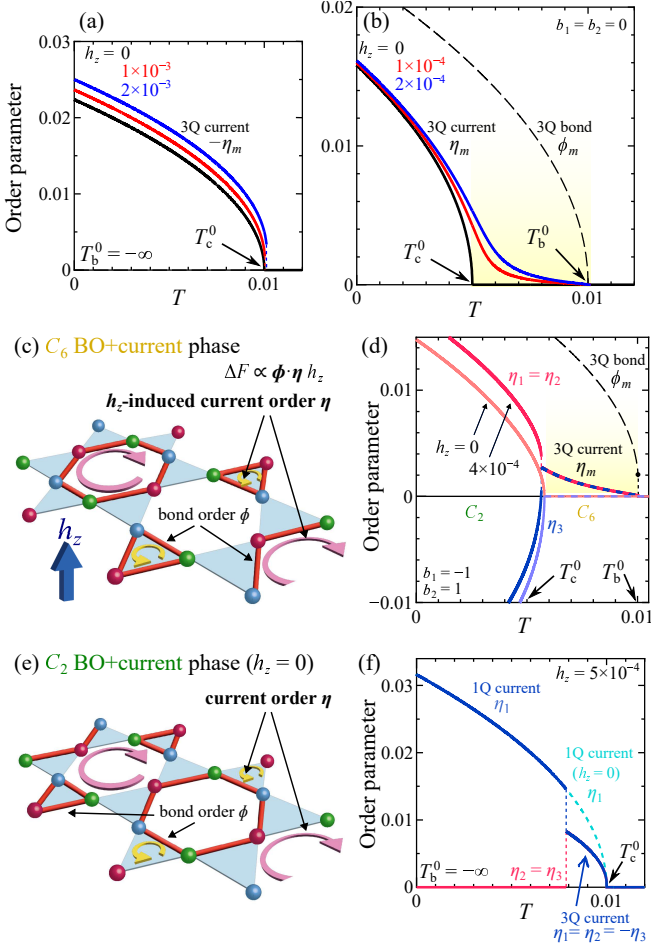


FIG. 4: (a)(b) Obtained 3Q current order  $\eta = (\eta_1, \eta_2, \eta_3)$  with  $\eta_1 = \eta_2 = \eta_3$  for  $2d_1/d_2 = 2$ ,  $2d_3/d_4 = 2$  and  $b_1 = b_2 = 0$  under  $h_z$ .  $h_z = 10^{-4}$  corresponds to 1 Tesla. (a) 3Q current order for  $T_c^0 = 0.01$  and  $T_b^0 = -\infty$ . The first-order transition is induced by  $h_z$  due to  $m_2$ -term. (b) 3Q current order for  $T_c^0 = 0.005$  under the 3Q BO  $\phi \propto (1, 1, 1)$  with  $T_b^0 = 0.01$ . For  $h_z \neq 0$ ,  $\eta$  starts to increase below  $T_b$  thanks to  $m_1$ -term, *i.e.*,  $T_c = T_b^0$ . (c)  $h_z$ -induced  $C_6$ -symmetry bond+current order above  $T_c^0$  the shaded area in (b). (d) 3Q current order for  $-b_1 = b_2 = 1.0$ . Other model parameters are equal to (b). The symmetry of the bond+current coexisting state is  $C_6$  ( $\eta_1 = \eta_2 = \eta_3$ ) for  $T > T_c^0$ , while  $C_2$  ( $\eta_1 = \eta_2 \approx -\eta_3$ ) for  $T < T_c^0$ . (e) Bond+current coexisting state below  $T_b^0$ . It has  $C_2$  symmetry to gain the 3rd order GL terms. (f) Obtained current order  $\eta_m$  for  $2d_3/d_4 = 1/1.2$  at  $T_c^0 = 0.01$  and  $h_z = 5 \times 10^{-4}$ , for  $T_b^0 = -\infty$ . The 3Q current order appears due to the  $m_2$ -term, while it changes to 1Q order at  $T \approx 0.008$ .

coexisting state above  $T_c^0$  is shown in Fig. 4 (c). Below  $T_c^0$ , the coexisting state changes to the nematic ( $C_2$ ) bond+current state shown in Figure 4 (e). We stress that  $\text{sgn}(\eta_1\eta_2\eta_3)$  changes at  $T \approx T_c^0$ . To summarize, the  $h_z$ -induced coexisting state changes its symmetry from  $C_6$  ( $T > T_c^0$ ) to  $C_2$  ( $T < T_c^0$ ) with decreasing  $T$ . The field-induced first-order phase transition occurs at  $T \approx T_c^0$ .

## $h_z$ -effect on 1Q current order state

In this section, we explain that the 1Q current order state is also drastically modified by  $h_z$ . Here, we increase  $d_4 = 150$  to 360 (*i.e.*,  $2d_3/d_4 = 1/1.2$ ) in the previous GL parameters. A clear evidence of the 1Q current order has been reported recently in Ref. [21]. We set  $T_c^0 = 0.01$ . Figure 4 (f) shows the obtained order parameters without BO ( $T_b^0 = -\infty$ ) at  $h_z = 5 \times 10^{-4}$ . We obtain the field-induced 3Q-current order due to the  $m_2$ -term, while it changes to 1Q order at  $T \approx 0.008$ . The field-induced first-order transitions reported in Ref. [21] would originate from the 1Q current order at  $T^{**}$  ( $> T_b^0$ ) together with  $\Delta\bar{F}$ . In Fig. 4 (f), we set  $2d_3/d_4 = 1.2$  and  $m_2 = 1000$ . The obtained  $h_z$ -induced 3Q current order is realized even when  $m_2 \approx 100$  when  $2d_3/d_4 \gtrsim 1$ .

In Fig. 4 (f), we set  $T_b^0 = -\infty$  for simplicity. However,  $T_b^0 \approx 0.01$  ( $\approx 100$  K) experimentally. In this case, as revealed in Ref. [9], the 3Q current order induces the finite 3Q BO even above  $T_b^0$  via the  $b_2$  term. This fact means that the 3Q current order is energetically favorable when  $b_2 \neq 0$ . Therefore,  $h_z$ -induced transition from 1Q to 3Q current order shown in Fig. 4 (f) can emerge even if  $2d_3/d_4 \lesssim 1$  for  $b_2 \neq 0$ .

For reference, we studied the case of the intra-original-unit-cell current order ( $\mathbf{q} = \mathbf{0}$ ) in kagome lattice in the SI G [49]. In this case,  $M_{\text{orb}}$  is  $\eta$ -linear even if the BO is absent.

## Derivation of GL coefficients based on the first-principles kagome metal model

In the next stage, we calculate the GL coefficients based on the first-principles tight-binding model for kagome metals. We reveal that  $|m_1|$  and  $|m_2|$  becomes large due to the “inter-orbital ( $d_{XZ} + d_{YZ}$ ) mixture” even if the current order emerges only in the  $d_{XZ}$ -orbital.

First, we derive 30-orbital (15  $d$ -orbital and 15  $p$ -orbitals) tight-binding model for  $\text{CsV}_3\text{Sb}_5$  by using WIEN2k and Wannier90 softwares. Figure 5 (a) shows the FS of the obtained model in the  $k_z = 0$  plane. (Its bandstructure is shown in Fig. S9 (a).) The  $d_{XZ}$ -orbital “pure-type” FS corresponds to the FS of the present three-orbital model. Its vHS energy is located at  $E_{\text{vHS}}^{XZ} \approx -0.1$ . Also, the  $d_{YZ}$ -orbital forms the “mix-type” FS whose vHS energy is  $E_{\text{vHS}}^{YZ} \approx +0.1$ . In addition, both  $d_{X^2-Y^2}$  and  $d_{3Z^2-R^2}$  orbitals form one pure-type band with the vHS energy  $E_{\text{vHS}}^{X^2-Y^2} \approx 0$ .

Figure 5 (b) shows the FS with introducing the  $p$ -orbital shift  $\Delta E_p = -0.2$  eV. Its bandstructure is shown in Fig. S9 (b). Here, the  $d_{YZ}$ -orbital (mix-type) FS approaches the M point, and its vHS point shifts to the Fermi level, consistently with the ARPES measurement in Ref. [42]. Figure 5 (c) shows the change in the FS topology due to the pure-mix hybridization in

the  $E_p = -0.2$  model for  $n = 30.48 \sim 31.00$ . When  $n = n_{\text{vHS}}^{\text{XZ}}$  ( $= 30.48$ ), we obtain two hole-pockets that attach the M point. With increasing  $n$ , it changes to the electron-like Dirac pockets at  $n \approx n_{\text{D}}$  ( $= 30.66$ ), composed of both  $d_{\text{XZ}}$  and  $d_{\text{YZ}}$  orbitals. At  $n = n_{\text{L}}$  ( $= 30.76$ ), large hole-like pure-type FS and large electron-like mix-type FS are formed. At  $n = 31$ , the mix-type FS lines on the M-M' line. We will see that large  $|m_1|$  and  $|m_2|$  appear at  $n \approx n_{\text{vHS}}$ ,  $n_{\text{D}}$  and 31.

Figure 5 (d) shows the obtained  $m_2(\mathbf{k})$  with the folded FSs. For both  $n = n_{\text{D}}$  and 31, the pure-mix hybridization contributes to the large GL coefficient in the 30-orbital model. This mechanism is absent in the simple single orbital model.

We note that  $E_{\text{vHS}}^{\text{XZ}} \approx 0$  is reported in an ARPES study for pristine  $\text{CsV}_3\text{Sb}_5$  in Ref. [45]. In this case, both  $m_1$  and  $m_2$  become very large theoretically.

Now, we calculate  $m_1$  and  $m_2$  in  $\bar{M}_{\text{orb}}$  by introducing the current and bond orders on the  $d_{\text{XZ}}$  orbitals in the 30-orbital kagome lattice model given in Figs. 5 (a) ( $\Delta E_p = 0$ ) and (b) ( $\Delta E_p = -0.2$ ). We derive the coefficients  $m_1$  and  $m_2$  defined as  $\bar{M}_{\text{orb}} = m_1 \tilde{\phi} \cdot \tilde{\eta} + m_2 \tilde{\eta}_1 \tilde{\eta}_2 \tilde{\eta}_3$ , where  $\tilde{\eta}_i$  and  $\tilde{\phi}_i$  are the  $d_{\text{XZ}}$ -orbital order parameters projected on the pure-type band. (We set  $\tilde{\eta}_i = \eta_i W_{\text{XZ}}$  and  $\tilde{\phi}_i = \phi_i W_{\text{XZ}}$  with  $W_{\text{XZ}} = 0.7$ , which is the  $d_{\text{XZ}}$ -weight on the pure-type band.)

The obtained  $m_1$  is shown in Figs. 5 (e) ( $\Delta E_p = 0$ ) and (f) ( $\Delta E_p = -0.2$ ), as function of the electron filling  $n$ . Here,  $m_{1(2)}$  is derived from the  $k_z = 0$  plane electronic structure. First, we discuss the case  $n = 31$  that corresponds to undoped  $\text{CsV}_3\text{Sb}_5$ . In both Figs. 5 (e) and (f), the obtained  $m_1$  is very larger for  $n \approx n_{\text{vHS}}^{\text{XZ}}$  ( $< 31$ ). At  $n = 31$ ,  $m_1$  in Fig. 5 (e) is relatively small ( $\sim -0.5$ ) accidentally, while its magnitude becomes large ( $m_1 \sim -2$ ) in Fig. 5 (f), where the mix-type FS is closer to the M-M' line. In fact, the mix-type FS contains finite  $d_{\text{XZ}}$ -weight ( $\sim 10\%$ ) owing to the inter-orbital mixture in kagome metal bandstructure. For this reason, the mix-type band can cause large  $M_{\text{orb}}$  even if the current order parameter occurs only in  $d_{\text{XZ}}$ -orbital. Thus, the current-bond-field trilinear coupling due to  $m_1$  term will cause the drastic field-induced chiral current order shown in Fig. 4 (b). This is the main result of this study.

The obtained  $m_2$  is shown in Figs. 5 (g) ( $\Delta E_p = 0$ ) and (h) ( $\Delta E_p = -0.2$ ), at  $T = 0.01$  and 0.005. The obtained  $m_2$  is extremely larger for  $n \approx n_{\text{vHS}}^{\text{XZ}}$  ( $< 31$ ). At  $n = 31$ ,  $m_2$  becomes relatively small ( $\sim -50$ ) in Fig. 5 (g). However,  $m_2$  increases to  $\sim 400$  in Fig. 5 (h) because the mix-type FS is closer to the M-M' line. Thus, large  $|m_2|$  can be realized by the mix-type band with finite  $d_{\text{XZ}}$ -orbital weight even when  $|E_{\text{vHS}}^{\text{XZ}} - \mu| \sim 0.1$ . We stress that the relation  $m_2 \approx -m_3$  is well satisfied; see the SI B [49].

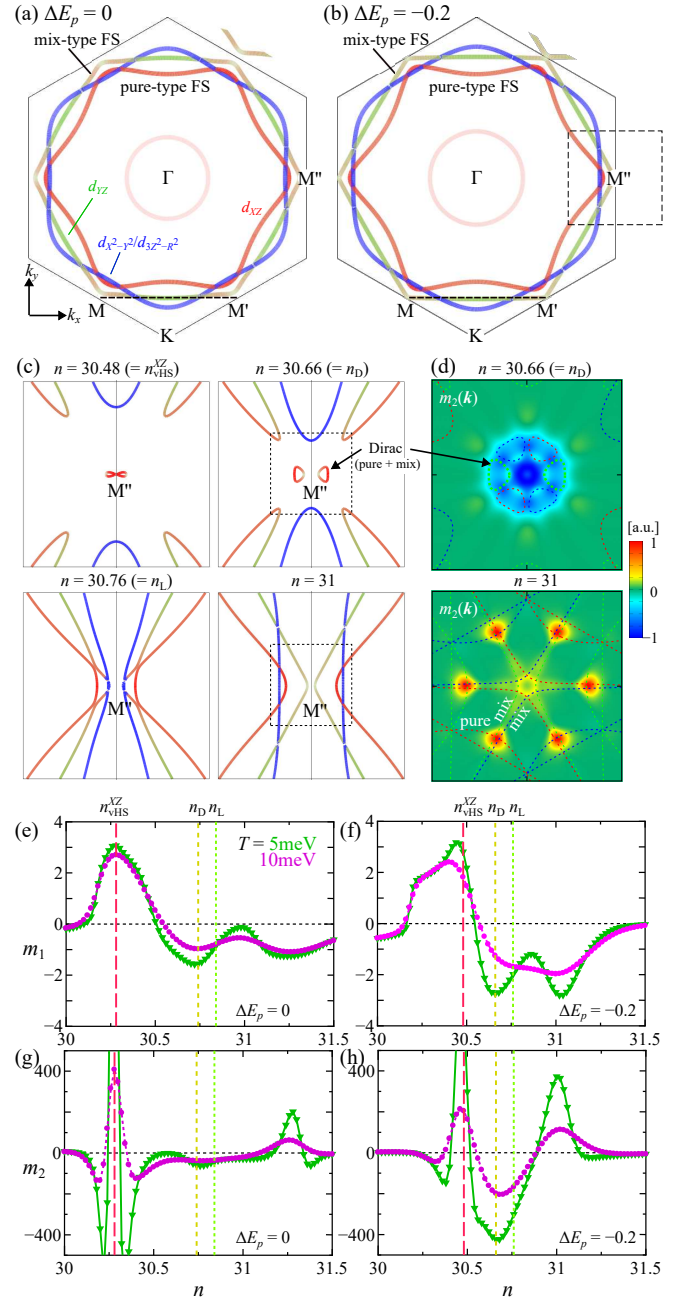


FIG. 5: (a) FS of  $\text{CsV}_3\text{Sb}_5$  model in the  $k_z = 0$  plane. The  $d_{\text{XZ}}$ -orbital band gives the pure-type FS, and the  $d_{\text{YZ}}$ -orbital band gives the mix-type FS. The  $d_{\text{X}^2-\text{Y}^2} + d_{\text{3Z}^2-\text{R}^2}$ -orbital band gives another pure-type FS. (b) FS with the  $p$ -orbital shift  $\Delta E_p = -0.2$  eV. Here, the mix-type FS is closer to the M points. (c) Change in the FS topology with  $n$  in  $E_p = -0.2$  model inside the dashed line square in (b) (d)  $m_2(\mathbf{k})$  inside the dotted line square in (c). with the folded FSs at  $n = n_{\text{D}}$  and  $n = 31$ . (e-h) Obtained  $m_n$  at  $T = 0.01$  and 0.005: (e)  $m_1$  in  $\Delta E_p = 0$  model, where  $m_1 \sim -0.5$  at  $n = 31$ . (f)  $m_1$  in  $\Delta E_p = -0.2$  model, where  $m_1 \sim -2$  at  $n = 31$ . (g)  $m_2$  in  $\Delta E_p = 0$  model, where  $m_2 \sim -50$  at  $n = 31$ . (h)  $m_2$  in  $\Delta E_p = -0.2$  model, where  $m_2 \sim 300$  at  $n = 31$ .

Next, we discuss the  $n$ -dependences of  $m_1$  and  $m_2$  in more detail. In Figs. 5 (e)-(h), both coefficients take very large values at  $n \approx n_{\text{vHS}}^X$  due to the hybridization between  $d_{XZ}$ -orbital bands, as we explained in Fig. 3. With increasing  $n$ , these coefficients exhibit drastic  $n$ -dependences when the FS changes its topology due to the pure-mix hybridization. When  $n \approx n_D$ , the electron-like Dirac pockets made of  $d_{XZ} + d_{YZ}$  orbitals cause large  $|m_1|$  and  $|m_2|$ .  $|m_1|$  and  $|m_2|$  are also enlarged when the mix-band (with finite  $d_{XZ}$ -weight) is close to the M-M' line at  $n \approx 31$  in  $\Delta E_p = -0.2$  model [at  $n \approx 31.2$  in  $\Delta E_p = 0$  model].

To summarize, both  $m_1$  and  $m_2$  exhibit interesting sensitivity to the multiorbital character and the nesting condition of the bandstructure around M points. Unexpectedly, both  $d_{XZ}$ -orbital (pure-type) band and  $d_{YZ}$ -orbital (mix-type) band play important role for  $m_1$  and  $m_2$  even when the current order emerges only on the  $d_{XZ}$ -orbital. When  $\Delta E_p = -0.2$ , the mix-type FS approaches the M point, consistently with the ARPES bandstructure [42]. Then, we obtain large  $|m_1| (\sim 2)$  and  $|m_2| (\lesssim 400)$  at  $n = 31$  as shown in Figs. 5 (f) and (h). Thus, the  $h_z$ -induced change in Fig. 4 can be obtained by changing the parameters slightly. (“Nearly commensurate” current order may appear in  $\Delta E_p = 0$  model, in which the nesting of the FS at  $\mathbf{q}_m$  is not perfect [11]. The calculated  $m_n$  will be larger by using the correct incommensurate nesting vector of  $\Delta E_p = 0$  model. ) In the SI H [49], we calculate the GL coefficients when the current and bond orders emerge on other  $d$ -orbitals. It is found that large  $m_1$  and  $m_2$  are obtained in various cases. Thus, the present study is valid for various types of current order mechanisms, not restricted to Ref. [35].

### Summary and Discussions

In summary, the chiral current order in kagome metal exhibits weak ferromagnetism, and its magnitude are enlarged in the bond order state. Importantly, we derived the  $h_z$ -induced GL free energy expression  $\Delta \bar{F}$  in Eq. [9], which provides an important basis for future research in kagome metals. The emergent  $\eta \cdot \phi \cdot h_z$  trilinear term in  $\Delta \bar{F}$  explains prominent field-induced chiral symmetry breaking in kagome metals. We revealed that  $m_n$  becomes large when the vHS energy is close to the Fermi level because the prominent FS reconstruction occurs due to the current order parameters. Furthermore, the multi-orbital mixing in the bandstructure of real kagome metals makes  $m_n$  larger for a wide filling range. The finding that  $m_n$  sensitively depends on the multiorbital bandstructure in Fig. 5 provides a useful hint to control the charge current or to understand the difference between Cs-based and K-based compounds [51]. Interestingly, we obtain large  $m_n$  when the current order parameter emerges in not only  $d_{XZ}$ -orbital, but also other  $d$ -orbitals. It is in-

teresting to study  $m_n$  for theoretically proposed exotic TRS breaking states, such as the inter-orbital exciton order [39] and multipolar and toroidal magnetic orders [37].

Below, we discuss several important issues.

### Comparison with experiments: $h_z$ -induced current order

In Ref. [41], it was proposed that  $\text{CsV}_3\text{Sb}_5$  is located at the quantum critical point of the current order ( $\bar{T}_c^0 \approx 0$ ) in the absence of the uniaxial strain. (As we discussed above,  $T_c^0$  is renormalized to  $\bar{T}_c^0$  under the BO phase.) The field-induced ( $h_z \sim 9\text{T}$ ) current order at  $T \sim 20\text{K}$  is naturally understood based on the GL free energy analysis with the current-bond- $h_z$  trilinear term. Figures 4 (b) and (d) corresponds to the experimental report in Ref. [41] by considering that  $\bar{T}_c^0 \approx 0$ . In addition, the present GL theory explains the field-induced enhancement of the local magnetic flux ( $\propto \eta^1$ ) observed by  $\mu\text{SR}$  measurements in  $\text{AV}_3\text{Sb}_5$  [15–17] and field-tuned chiral transport study [20]. Interestingly, the obtained  $m_n$  sensitively depends on the multiorbital bandstructure and the filling in Fig. 5 (and Fig. S9). The present discovery provides a useful hint to control the charge current in kagome metals. The present finding will also be essential to understand the significant difference between Cs-based and K-based compounds reported in Ref. [51]. In addition, the discovery of CDW state in double-layer kagome metal  $\text{ScV}_6\text{Sn}_6$  [52] has attracted increasing theoretical interest [38, 53, 54]. The TRS breaking state and its increment under  $h_z$  discovered in  $\text{ScV}_6\text{Sn}_6$  [55] may be understood by developing the present GL theory.

We note that the trilinear term in  $\Delta \bar{F}$  is also caused by the spin magnetization in the presence of spin-orbit interaction [37]. Future quantitative calculations would be important.

### Comparison with experiments: Strain-induced current order

Reference [41] also reports interesting prominent strain induced increment of  $\bar{T}_c^0$ . Under the uniaxial strain, the degeneracy of the current order transition temperature at  $\mathbf{q} = \mathbf{q}_m$  ( $m = 1 \sim 3$ ),  $\bar{T}_c^{(m)}$ , is lifted by the change in the 2nd order GL term as discussed in Ref. [41]. Then,  $\bar{T}_c = \max_m \bar{T}_c^{(m)}$  will be larger than the original  $\bar{T}_c^0$ . In the SI I [49], we find that additional significant contribution to the increment of  $\bar{T}_c^0$  originates from the strain induced change in the 4th order GL terms ( $d_i$ ). Here, the “BO-induced suppression of the current order by  $d_5$  and  $d_6$  GL terms is found to be drastically



reduced by the strain. In fact, we find that  $d_i$  is sensitive to the strain because the vHS energy is close to the Fermi level; see Fig. S10 in the SI I [49].

Below, we explain the discussion in the SI I [49]. Considering the  $D_{6h}$  symmetry, we assume that the  $E_{1g}$  symmetry strain  $(\epsilon, \epsilon')$  induces the shift of the vHS energy levels as  $\Delta \mathbf{E} \equiv (\Delta E_A, \Delta E_B, \Delta E_C) = \alpha(\epsilon, 0, -\epsilon)$ . ( $\Delta \mathbf{E}'$  by  $\epsilon'$  is presented in the SI I [49].) Hereafter, we set  $\alpha = 1$ . Under the 3Q BO phase  $\phi^0 = (\phi^0, \phi^0, \phi^0)/\sqrt{3}$ , the 2nd order GL coefficient  $a_c$  in Eq. [11] in the absence of the strain ( $\epsilon = 0$ ) is changed to

$$\begin{aligned} \bar{a}_c(0) &= a_c + 2(d^5 + d^6)((\phi^0)^2/3) \\ &\propto T - \bar{T}_c^0, \end{aligned} \quad (14)$$

where  $|\phi^0| \gtrsim T_b$  when  $T \ll T_b$ . Here, we assume that  $\phi^0$  is  $T$ -independent because we study the strain-induced current order for  $T \ll T_b^0$ . For finite  $\epsilon$ , it is changed by  $\Delta F(\epsilon)$  as

$$\begin{aligned} \bar{a}_c(\epsilon) &= \bar{a}_c^0 - [(2g_5 + g_6) + D(2g_1 + g_2)]((\phi^0)^2/6) \\ &\propto T - \bar{T}_c(\epsilon), \end{aligned} \quad (15)$$

where  $g_l$  are  $\epsilon$ -linear. Here,  $\bar{T}_c(0) = \bar{T}_c^0$ .  $g_l$  and  $d_l^{(m)}$  are related as  $\epsilon \cdot (\partial_\epsilon d_l^{(1)}, \partial_\epsilon d_l^{(2)}, \partial_\epsilon d_l^{(3)}) = (-1)^l \cdot g_l(1, -1, 0)$ . The current order appears in the BO phase when Eq. [15] becomes negative. Therefore,  $\bar{T}_c(\epsilon)$  will increase in proportion to  $\epsilon$  if  $(2g_5 + g_6) > 0$ . Therefore, we obtain  $\bar{T}_c(\epsilon) \sim (\epsilon/\epsilon_0)(\bar{T}_c^0 - \bar{T}_c^0)$  with  $\epsilon_0 = 0.025$  (0.029) for  $n = 2.56$  (2.48), according to the numerical study in Fig. S10. This increment of  $\bar{T}_c(\epsilon)$  originates from the reduction of the BO-induced suppression of the current order. Therefore, considering that  $\bar{T}_c^0 \sim 0.01$  and  $\bar{T}_c^0 = 0$  (= at current order QCP), we obtain  $\bar{T}_c(\epsilon) \sim 0.002$  ( $\approx 20$  K) at  $\epsilon \sim 0.005$  ( $\approx 50$  K). Based on this extrinsic strain scenario, one may understand the difference of  $T_c$  by experiments, such as the absence of the TRS breaking at  $h_z = 0$  reported by Kerr rotation study [22].

### Nematic 3D stacking 3Q BO and current order

As revealed in Ref. [9], the nematic state can be realized by the  $\pi$ -shift 3D stacking of the 3Q BO thanks to the 3rd order GL term  $b_1$ . This state is the combination of three BO states at wavevectors  $\mathbf{q}_l^{3D} = (\mathbf{q}_l^{2D}, q_l^z)$  for  $l = 1, 2, 3$  ( $\mathbf{q}_l^{2D}$  is shown in Fig. 1 (a)) when  $\{q_1^z, q_2^z, q_3^z\} = \{\pi, \pi, 0\}$ ,  $\{\pi, 0, \pi\}$  or  $\{0, \pi, \pi\}$ . Because of the relation  $\sum_l^{1,2,3} \mathbf{q}_l^{3D} = \mathbf{0}$ , the  $\pi$ -shift stacking gains the 3rd order GL free energy due to the  $b_1$  term. Its necessary condition is that the 2nd order GL term  $a_b$  is almost  $q_z$ -independent. Consistently, we recently find that the DW equation eigenvalue for the BO,  $\lambda_\phi(\mathbf{q}_l^{2D}, q^z)$ , is almost  $q_z$ -independent by reflecting almost 2D character of 3D 30-orbital  $\text{CsV}_3\text{Sb}_5$  model [56]. (Note that

$a_b \propto (-1 + \lambda_\phi^{-1})$ .) In contrast, the  $q_z$ -dependence of  $b_1$  is rather prominent [56]. Thus, we expect that the nematic 3Q BO state discussed in Ref. [9] is realistic.

Next, we discuss the 3D structure of the field-induced 3Q current order. In the absence of the BO, by the same argument as above, the 3Q current order will form the  $\pi$ -shift stacking to gain the  $m_2$ -term contribution in  $\Delta \bar{F}$ . When the 3Q current order appears inside the 3Q BO state, the 3D stacking of the current order would be mainly determined by the 3rd order GL term  $b_2$  that describes the bond-current coupling energy.

### Derivation of $E_0$

The expressions of orbital magnetization derived by Refs. [46, 47] is given as

$$M_{\text{orb}} = \frac{ea^2}{2c\hbar N_{\text{uc}} N} \sum_{\mathbf{k}\sigma} m(\mathbf{k}),$$

where  $m(\mathbf{k})$  is given in Eq. [4].  $a$  is the unit length in this numerical calculation. Here, we set  $a = |\mathbf{a}_{\text{AB}}|$ .  $N_{\text{uc}}$  is the site number of the unit cell,  $N$  is the  $\mathbf{k}$ -mesh number. By using the  $\mu_B = \frac{e\hbar}{2m_e c}$  and  $E_0 \equiv \frac{\hbar^2}{m_e a^2}$ , we obtain Eq. [3]. By using the  $m_e c^2 = 0.511 \times 10^6$  [eV] and  $\frac{\hbar}{m_e c} = 3.86 \times 10^{-13}$  [m], we obtain  $E_0 = 0.5$  [eV] for  $a = 0.4$  [nm]. In Kagome metals ( $a = 0.275$  [nm]),  $E_0 = 1.0$  [eV]. In the numerical calculation, large number of  $N$  is required to obtain a reliable result at low temperatures. Here, we set  $N = (2400)^2$  at  $T = 1$  [meV].

### Acknowledgments

We are grateful to Y. Matsuda, T. Shibauchi, K. Hashimoto, T. Asaba, S. Onari, A. Ogawa and K. Shimura for fruitful discussions. This study has been supported by Grants-in-Aid for Scientific Research from MEXT of Japan (JP20K03858, JP20K22328, JP22K14003), and by the Quantum Liquid Crystal No. JP19H05825 KAKENHI on Innovative Areas from JSPS of Japan.

- 
- [1] B. R. Ortiz, L. C. Gomes, J. R. Morey, M. Winiarski, M. Bordelon, J. S. Mangum, I. W. H. Oswald, J. A. Rodriguez-Rivera, J. R. Neilson, S. D. Wilson, E. Ertekin, T. M. McQueen, and E. S. Toberer, *New kagome prototype materials: discovery of  $\text{KV}_3\text{Sb}_5$ ,  $\text{RbV}_3\text{Sb}_5$ , and  $\text{CsV}_3\text{Sb}_5$* , Phys. Rev. Materials **3**, 094407 (2019).
- [2] B. R. Ortiz, S. M. L. Teicher, Y. Hu, J. L. Zuo, P. M. Sarte, E. C. Schueller, A. M. M. Abeykoon, M. J. Krogstad, S. Rosenkranz, R. Osborn, R. Seshadri, L. Balents, J. He, and S. D. Wilson,  *$\text{CsV}_3\text{Sb}_5$ : A  $\mathbb{Z}_2$  Topologi-*

- cal Kagome Metal with a Superconducting Ground State*, Phys. Rev. Lett. **125**, 247002 (2020).
- [3] Y.-X. Jiang, J.-X. Yin, M. M. Denner, N. Shumiya, B. R. Ortiz, G. Xu, Z. Guguchia, J. He, M. S. Hossain, X. Liu, J. Ruff, L. Kautzsch, S. S. Zhang, G. Chang, I. Belopolski, Q. Zhang, T. A. Cochran, D. Multer, M. Litskevich, Z.-J. Cheng, X. P. Yang, Z. Wang, R. Thomale, T. Neupert, S. D. Wilson, and M. Z. Hasan, *Unconventional chiral charge order in kagome superconductor  $KV_3Sb_5$* , Nat. Mater. **20**, 1353 (2021).
- [4] H. Li, H. Zhao, B. R. Ortiz, T. Park, M. Ye, L. Balents, Z. Wang, S. D. Wilson, and I. Zeljkovic, *Rotation symmetry breaking in the normal state of a kagome superconductor  $KV_3Sb_5$* , Nat. Phys. **18**, 265 (2022).
- [5] M. L. Kiesel, C. Platt, and R. Thomale, *Unconventional Fermi Surface Instabilities in the Kagome Hubbard Model*, Phys. Rev. Lett. **110**, 126405 (2013).
- [6] W.-S. Wang, Z.-Z. Li, Y.-Y. Xiang, and Q.-H. Wang, *Competing electronic orders on kagome lattices at van Hove filling*, Phys. Rev. B **87**, 115135 (2013).
- [7] X. Wu, T. Schwemmer, T. Müller, A. Consiglio, G. Sangiovanni, D. Di Sante, Y. Iqbal, W. Hanke, A. P. Schnyder, M. M. Denner, M. H. Fischer, T. Neupert, and R. Thomale, *Nature of Unconventional Pairing in the Kagome Superconductors  $AV_3Sb_5$  ( $A = K, Rb, Cs$ )*, Phys. Rev. Lett. **127**, 177001 (2021).
- [8] M. M. Denner, R. Thomale, and T. Neupert, *Analysis of Charge Order in the Kagome Metal  $AV_3Sb_5$  ( $A = K, Rb, Cs$ )*, Phys. Rev. Lett. **127**, 217601 (2021).
- [9] T. Park, M. Ye, and L. Balents, *Electronic instabilities of kagome metals: Saddle points and Landau theory*, Phys. Rev. B **104**, 035142 (2021).
- [10] Y.-P. Lin and R. M. Nandkishore, *Complex charge density waves at Van Hove singularity on hexagonal lattices: Haldane-model phase diagram and potential realization in the kagome metals  $AV_3Sb_5$  ( $A = K, Rb, Cs$ )*, Phys. Rev. B **104**, 045122 (2021).
- [11] R. Tazai, Y. Yamakawa, S. Onari, and H. Kontani, *Mechanism of exotic density-wave and beyond-Migdal unconventional superconductivity in kagome metal  $AV_3Sb_5$  ( $A = K, Rb, Cs$ )*, Sci. Adv. **8**, eabl4108 (2022).
- [12] M. Roppongi, K. Ishihara, Y. Tanaka, K. Ogawa, K. Okada, S. Liu, K. Mukasa, Y. Mizukami, Y. Uwatoko, R. Grasset, M. Konczykowski, B. R. Ortiz, S. D. Wilson, K. Hashimoto, and T. Shibauchi, *Bulk evidence of anisotropic  $s$ -wave pairing with no sign change in the kagome superconductor  $CsV_3Sb_5$* , Nat. Commun. **14**, 667 (2023).
- [13] W. Zhang, X. Liu, L. Wang, C. W. Tsang, Z. Wang, S. T. Lam, W. Wang, J. Xie, X. Zhou, Y. Zhao, S. Wang, J. Tallon, K. T. Lai, and S. K. Goh, *Nodeless superconductivity in kagome metal  $CsV_3Sb_5$  with and without time reversal symmetry breaking*, Nano Lett., **23**, 872 (2023).
- [14] L. Yu, C. Wang, Y. Zhang, M. Sander, S. Ni, Z. Lu, S. Ma, Z. Wang, Z. Zhao, H. Chen, K. Jiang, Y. Zhang, H. Yang, F. Zhou, X. Dong, S. L. Johnson, M. J. Graf, J. Hu, H.-J. Gao, and Z. Zhao, *Evidence of a hidden flux phase in the topological kagome metal  $CsV_3Sb_5$* , arXiv:2107.10714 (available at <https://arxiv.org/abs/2107.10714>).
- [15] C. Mielke, D. Das, J.-X. Yin, H. Liu, R. Gupta, Y.-X. Jiang, M. Medarde, X. Wu, H. C. Lei, J. Chang, P. Dai, Q. Si, H. Miao, R. Thomale, T. Neupert, Y. Shi, R. Khasanov, M. Z. Hasan, H. Luetkens, and Z. Guguchia, *Time-reversal symmetry-breaking charge order in a kagome superconductor*, Nature **602**, 245 (2022).
- [16] R. Khasanov, D. Das, R. Gupta, C. Mielke, M. Elender, Q. Yin, Z. Tu, C. Gong, H. Lei, E. T. Ritz, R. M. Fernandes, T. Birol, Z. Guguchia, and H. Luetkens, *Time-reversal symmetry broken by charge order in  $CsV_3Sb_5$* , Phys. Rev. Research **4**, 023244 (2022).
- [17] Z. Guguchia, C. Mielke, D. Das, R. Gupta, J.-X. Yin, H. Liu, Q. Yin, M. H. Christensen, Z. Tu, C. Gong, N. Shumiya, M. S. Hossain, T. Gamsakhurdashvili, M. Elender, P. Dai, A. Amato, Y. Shi, H. C. Lei, R. M. Fernandes, M. Z. Hasan, H. Luetkens, and R. Khasanov, *Tunable unconventional kagome superconductivity in charge ordered  $RbV_3Sb_5$  and  $KV_3Sb_5$* , Nat. Commun. **14**, 153 (2023).
- [18] Y. Xu, Z. Ni, Y. Liu, B. R. Ortiz, Q. Deng, S. D. Wilson, B. Yan, L. Balents, and L. Wu, *Three-state nematicity and magneto-optical Kerr effect in the charge density waves in kagome superconductors*, Nat. Phys. **18**, 1470 (2022).
- [19] Y. Hu, S. Yamane, G. Mattoni, K. Yada, K. Obata, Y. Li, Y. Yao, Z. Wang, J. Wang, C. Farhang, J. Xia, Y. Maeno, and S. Yonezawa, *Time-reversal symmetry breaking in charge density wave of  $CsV_3Sb_5$  detected by polar Kerr effect*, arXiv:2208.08036 (available at <https://arxiv.org/abs/2208.08036>).
- [20] C. Guo, C. Putzke, S. Konyzheva, X. Huang, M. Gutierrez-Amigo, I. Errea, D. Chen, M. G. Vergniory, C. Felser, M. H. Fischer, T. Neupert, and P. J. W. Moll, *Switchable chiral transport in charge-ordered kagome metal  $CsV_3Sb_5$* , Nature **611**, 461 (2022).
- [21] T. Asaba *et al.*, unpublished.
- [22] D. R. Saykin, C. Farhang, E. D. Kountz, D. Chen, B. R. Ortiz, C. Shekhar, C. Felser, S. D. Wilson, R. Thomale, J. Xia, and A. Kapitulnik, *High Resolution Polar Kerr Effect Studies of  $CsV_3Sb_5$ : Tests for Time Reversal Symmetry Breaking Below the Charge Order Transition*, Phys. Rev. Lett. **131**, 016901 (2023).
- [23] F. D. M. Haldane, *Model for a Quantum Hall Effect without Landau Levels: Condensed-Matter Realization of the "Parity Anomaly"*, Phys. Rev. Lett. **61**, 2015 (1988).
- [24] S.-Y. Yang, Y. Wang, B. R. Ortiz, D. Liu, J. Gayles, E. Derunova, R. Gonzalez-Hernandez, L. Šmejkal, Y. Chen, S. S. P. Parkin, S. D. Wilson, E. S. Toberer, T. McQueen, and M. N. Ali, *Giant, unconventional anomalous Hall effect in the metallic frustrated magnet candidate,  $KV_3Sb_5$* , Sci. Adv. **6**, eabb6003 (2020).
- [25] F. H. Yu, T. Wu, Z. Y. Wang, B. Lei, W. Z. Zhuo, J. J. Ying, and X. H. Chen, *Concurrence of anomalous Hall effect and charge density wave in a superconducting topological kagome metal*, Phys. Rev. B **104**, L041103 (2021).
- [26] S. Onari and H. Kontani, *Self-consistent Vertex Correction Analysis for Iron-based Superconductors: Mechanism of Coulomb Interaction-Driven Orbital Fluctuations*, Phys. Rev. Lett. **109**, 137001 (2012).
- [27] Y. Yamakawa, S. Onari, and H. Kontani, *Nematicity and Magnetism in  $FeSe$  and Other Families of Fe-Based Superconductors*, Phys. Rev. X **6**, 021032 (2016).
- [28] S. Onari and H. Kontani,  *$SU(4)$  Valley+Spin Fluctuation Interference Mechanism for Nematic Order in Magic-Angle Twisted Bilayer Graphene: The Impact of Vertex Corrections*, Phys. Rev. Lett. **128**, 066401 (2022).
- [29] M. Tsuchiizu, Y. Ohno, S. Onari, and H. Kontani, *Orbital Nematic Instability in the Two-Orbital Hubbard Model: Renormalization-Group + Constrained RPA Analysis*,

- Phys. Rev. Lett. **111**, 057003 (2013).
- [30] M. Tsuchiizu, K. Kawaguchi, Y. Yamakawa, and H. Kontani, *Multistage electronic nematic transitions in cuprate superconductors: A functional-renormalization-group analysis*, Phys. Rev. B **97**, 165131 (2018).
- [31] A. V. Chubukov, M. Khodas, and R. M. Fernandes, *Magnetism, Superconductivity, and Spontaneous Orbital Order in Iron-Based Superconductors: Which Comes First and Why?*, Phys. Rev. X **6**, 041045 (2016).
- [32] R. M. Fernandes, P. P. Orth, and J. Schmalian, *Intertwined Vestigial Order in Quantum Materials: Nematicity and Beyond*, Annu. Rev. Condens. Matter Phys. **10**, 133 (2019).
- [33] H. Kontani, R. Tazai, Y. Yamakawa, and S. Onari, *Unconventional density waves and superconductivities in Fe-based superconductors and other strongly correlated electron systems*, Adv. Phys. **70**, 355 (2021).
- [34] J. C. S. Davis and D.-H. Lee, *Concepts relating magnetic interactions, intertwined electronic orders, and strongly correlated superconductivity*, Proc. Natl. Acad. Sci. U.S.A. **110**, 17623 (2013).
- [35] R. Tazai, Y. Yamakawa, and H. Kontani, *Charge-loop current order and Z<sub>3</sub> nematicity mediated by bond-order fluctuations in kagome metal AV<sub>3</sub>Sb<sub>5</sub> (A=Cs,Rb,K)*, arXiv:2207.08068 (available at <https://arxiv.org/abs/2207.08068>).
- [36] S. Zhou and Z. Wang, *Chern Fermi pocket, topological pair density wave, and charge-4e and charge-6e superconductivity in kagomé superconductors*, Nat. Commun. **13**, 7288 (2022).
- [37] M. H. Christensen, T. Biro, B. M. Andersen, and R. M. Fernandes, *Loop currents in AV<sub>3</sub>Sb<sub>5</sub> kagome metals: Multipolar and toroidal magnetic orders*, Phys. Rev. B **106**, 144504 (2022)
- [38] F. Grandi, A. Consiglio, M. A. Sentef, R. Thomale, and D. M. Kennes, *Theory of nematic charge orders in kagome metals*, Phys. Rev. B **107**, 155131 (2023)
- [39] H. D. Scammell, J. Ingham, T. Li, and O. P. Sushkov, *Chiral excitonic order from twofold van Hove singularities in kagome metals*, Nat. Commun. **14**, 605 (2023)
- [40] L. Nie, K. Sun, W. Ma, D. Song, L. Zheng, Z. Liang, P. Wu, F. Yu, J. Li, M. Shan, D. Zhao, S. Li, B. Kang, Z. Wu, Y. Zhou, K. Liu, Z. Xiang, J. Ying, Z. Wang, T. Wu, and X. Chen, *Charge-density-wave-driven electronic nematicity in a kagome superconductor*, Nature **604**, 59 (2022).
- [41] C. Guo, G. Wagner, C. Putzke, D. Chen, K. Wang, L. Zhang, M. G. Amigo, I. Errea, M. G. Vergniory, C. Felser, M. H. Fischer, T. Neupert, and P. J. W. Moll, *Correlated order at the tipping point in the kagome metal CsV<sub>3</sub>Sb<sub>5</sub>*, arXiv:2304.00972.
- [42] Y. Hu, X. Wu, B. R. Ortiz, S. Ju, X. Han, J. Ma, N. C. Plumb, M. Radovic, R. Thomale, S. D. Wilson, A. P. Schnyder, and M. Shi, *Rich nature of Van Hove singularities in Kagome superconductor CsV<sub>3</sub>Sb<sub>5</sub>*, Nat. Commun. **13**, 2220 (2022).
- [43] Y. Luo, S. Peng, S. M. L. Teicher, L. Huai, Y. Hu, B. R. Ortiz, Z. Wei, J. Shen, Z. Ou, B. Wang, Y. Miao, M. Guo, M. Shi, S. D. Wilson, and J.-F. He, *Distinct band reconstructions in kagome superconductor CsV<sub>3</sub>Sb<sub>5</sub>*, Phys. Rev. B **105**, L241111 (2022).
- [44] Z. Liu, N. Zhao, Q. Yin, C. Gong, Z. Tu, M. Li, W. Song, Z. Liu, D. Shen, Y. Huang, K. Liu, H. Lei, and S. Wang, *Charge-Density-Wave-Induced Bands Renormalization and Energy Gaps in a Kagome Superconductor RbV<sub>3</sub>Sb<sub>5</sub>*, Phys. Rev. X **11**, 041010 (2021).
- [45] K. Nakayama, Y. Li, T. Kato, M. Liu, Z. Wang, T. Takahashi, Y. Yao, and T. Sato *Carrier Injection and Manipulation of Charge-Density Wave in Kagome Superconductor CsV<sub>3</sub>Sb<sub>5</sub>*, Phys. Rev. X **12**, 011001 (2022).
- [46] D. Ceresoli, T. Thonhauser, D. Vanderbilt, and R. Resta, *Orbital magnetization in crystalline solids: Multi-band insulators, Chern insulators, and metals*, Phys. Rev. B **74**, 024408 (2006).
- [47] J. Shi, G. Vignale, D. Xiao, and Q. Niu, *Quantum Theory of Orbital Magnetization and Its Generalization to Interacting Systems*, Phys. Rev. Lett. **99**, 197202 (2007).
- [48] R. Tazai, Y. Yamakawa, and H. Kontani, *Emergence of charge loop current in the geometrically frustrated Hubbard model: A functional renormalization group study*, Phys. Rev. B **103**, L161112 (2021).
- [49] Supplementary Information.
- [50] R. Tazai, S. Matsubara, Y. Yamakawa, S. Onari, and H. Kontani, *Rigorous formalism for unconventional symmetry breaking in Fermi liquid theory and its application to nematicity in FeSe*, Phys. Rev. B **107**, 035137 (2023).
- [51] C. Guo, M. R. Delft, M. G. Amigo, D. Chen, C. Putzke, G. Wagner, M. H. Fischer, T. Neupert, I. Errea, M. G. Vergniory, S. Wiedmann, C. Felser, P. J. W. Moll, *Distinct switching of chiral transport in the kagome metals KV<sub>3</sub>Sb<sub>5</sub> and CsV<sub>3</sub>Sb<sub>5</sub>*, arXiv:2306.00593.
- [52] H. W. S. Arachchige, W. R. Meier, M. Marshall, T. Matsumoto, R. Xue, M. A. McGuire, R. P. Hermann, H. Cao, and D. Mandrus, *Charge Density Wave in Kagome Lattice Intermetallic ScV<sub>6</sub>Sn<sub>6</sub>*, Phys. Rev. Lett. **129**, 216402 (2022).
- [53] A. Korshunov, H. Hu, D. Subires, Y. Jiang, D. Calugaru, X. Feng, A. Rajapitamahuni, C. Yi, S. Roychowdhury, M. G. Vergniory, J. Strempler, C. Shekhar, E. Vescovo, D. Chernyshov, A. H. Said, A. Bosak, C. Felser, B. A. Bernevig, and S. Blanco-Canosa, *Softening of a flat phonon mode in the kagome ScV<sub>6</sub>Sn<sub>6</sub>*, arXiv: 2304.09173.
- [54] H. Hu, Y. Jiang, D. Calug, X. Feng, D. Subires, M. G. Vergniory, C. Felser, S. Blanco-Canosa, and B. A. Bernevig, *Kagome Materials I: SG 191, ScV<sub>6</sub>Sn<sub>6</sub>. Flat Phonon Soft Modes and Unconventional CDW Formation: Microscopic and Effective Theory*, arXiv:2305.15469.
- [55] Z. Guguchia, D.J. Gawryluk, Sohyeon Shin, Z. Hao, C. Mielke III, D. Das, I. Plokhikh, L. Liborio, K. Shenton, Y. Hu, V. Sazgari, M. Medarde, H. Deng, Y. Cai, C. Chen, Y. Jiang, A. Amato, M. Shi, M.Z. Hasan, J.-X. Yin, R. Khasanov, E. Pomjakushina, and H. Luetkens, *Hidden magnetism uncovered in charge ordered bilayer kagome material ScV<sub>6</sub>Sn<sub>6</sub>*, arXiv:2304.06436.
- [56] S. Onari, R. Tazai, Y. Yamakawa, and H. Kontani, unpublished.

## [Supplementary Information]

# Drastic magnetic-field-induced chiral current order and emergent current-bond-field interplay in kagome metal $\text{AV}_3\text{Sb}_5$ ( $\text{A}=\text{Cs},\text{Rb},\text{K}$ )

Rina Tazai<sup>1\*</sup>, Youichi Yamakawa<sup>2\*</sup>, and Hiroshi Kontani<sup>2</sup>

<sup>1</sup>*Yukawa Institute for Theoretical Physics, Kyoto University, Kyoto 606-8502, Japan*

<sup>2</sup>*Department of Physics, Nagoya University, Nagoya 464-8602, Japan*

### A: Bandstructure with bond+current orders

In the main text, we study the orbital magnetization  $M_{\text{orb}}$  in the presence of the current and bond orders based on Eqs. [3] and [6] in the main text [1, 2].  $M_{\text{orb}}$  originates from the vertical p-h excitation between the occupied bands ( $\epsilon_{\alpha\mathbf{k}} < \mu$ ) and unoccupied bands ( $\epsilon_{\beta\mathbf{k}} > \mu$ ). In the present study,  $M_{\text{orb}}$  becomes finite in the presence of the TRSB order current order parameters. Thus, it is important to understand the change in the bandstructure due to the order parameters. Hereafter, the unit of energy is eV unless otherwise noted.

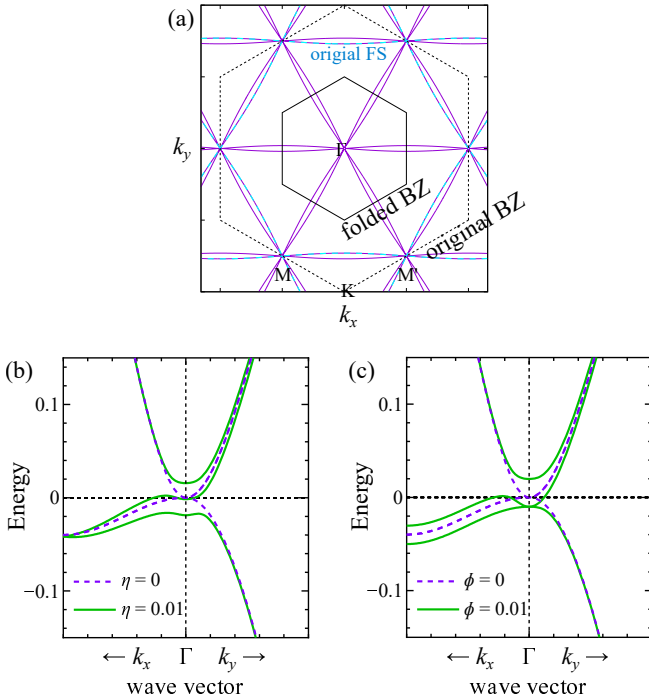


FIG. S1: (a) Folded FS at vHS filling for  $\phi = \eta = 0$ . (b)(c) Folded bandstructure in the presence of (b) the 3Q current order ( $\eta = 0, 0.01$ ) and (c) the 3Q BO ( $\phi = 0, 0.01$ ). Here, we set the origin of the energy at the vHS energy.

The folded FS at the vHS filling for  $\phi = \eta = 0$  is shown in Fig. S1 (a). Figure S1 (b) shows the folded bandstructure at  $n = n_{\text{vHS}}$  around  $\Gamma$  point in the presence of 3Q current order  $\boldsymbol{\eta} = (\eta, \eta, \eta)$  for  $\phi = 0$  and 0.01. Here, all vHS points A, B, C in Fig. 1 (b) move to  $\Gamma$  point, and they split into one bonding ( $\delta E = -\sqrt{3}\eta$ ), one antibonding ( $\delta E = \sqrt{3}\eta$ ), and one unhybridized ( $\delta E = 0$ ) states for finite  $\eta$ . (The bandstructure for 3Q BO  $\boldsymbol{\phi} = (\phi, \phi, \phi)$  is shown in Fig. S1 (c). The three vHS points split into two bonding ( $\delta E = -\phi$ ) and one antibonding ( $\delta E = 2\phi$ .)

In the bandstructure shown in Fig. S1 (a), the ‘‘vertical p-h excitations’’ (from  $\epsilon_{\alpha\mathbf{k}} < 0$  to  $\epsilon_{\beta\mathbf{k}} > 0$  for  $\mu = 0$ ) in the expression of  $M_{\text{orb}}$  are allowed in a wide  $\mathbf{k}$ -space for  $\mu \sim 0$ ; around  $\Gamma$ -M and M-M’ lines and around  $\Gamma$  and M points. Then, the factor  $(\epsilon_{\alpha\mathbf{k}} + \epsilon_{\beta\mathbf{k}} - 2\mu)^{-2}$  in the integrand of  $M_{\text{orb}}$  is  $O(\eta^{-2})$ , and the cancellation due to the factor  $(\epsilon_{\alpha\mathbf{k}} + \epsilon_{\beta\mathbf{k}} - 2\mu)$  is imperfect due to the p-h asymmetry. For this reason, large  $|M_{\text{orb}}|$  is realized at  $n \sim n_{\text{vHS}}$ .

### B: Relation $m_2 \approx -m_3$ , Expansion of $M_{\text{orb}}[\eta, \phi]$ based on the Green function method

In Fig. S2, we show the obtained  $m_2$  and  $-m_3$  in the (a) three-orbital kagome lattice model and (b) 30-orbital first-principles model. In both models, the relation  $m_2 \approx -m_3$  is well satisfied. For this reason, we present only  $m_1$  and  $m_2$  in the main text.

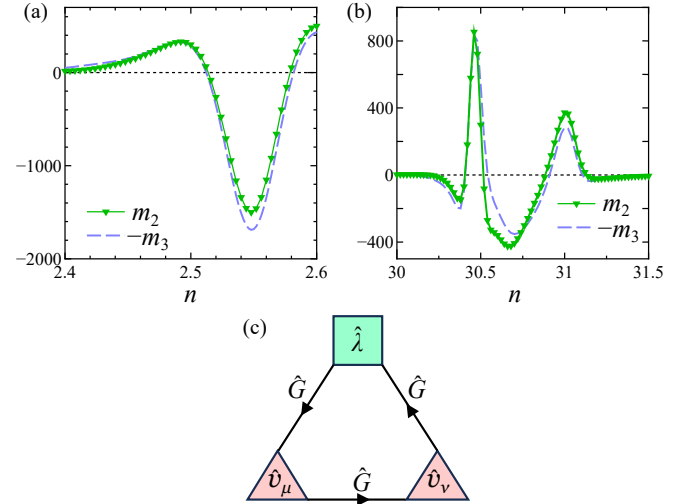


FIG. S2: Obtained  $m_2$  and  $-m_3$  in the (a) three-orbital kagome lattice model and (b) 30-orbital first-principles model with  $\Delta E_p = -0.2$ . (c) Diagrammatic expression of  $M_{\text{orb}}$  given in Eq. [S1].

To understand the approximate relation  $m_2 \approx -m_3$ , we consider the expansion of  $M_{\text{orb}}$  with respect to  $\boldsymbol{\eta}$  and  $\boldsymbol{\phi}$ ;  $M_{\text{orb}} = \sum b_{prq}^{p'q'r'} \eta_1^p \eta_2^q \eta_3^r \phi_1^{p'} \phi_2^{q'} \phi_3^{r'}$ . In this notation,

$m_2 = b_{111}^{000}$  and  $m_3 = b_{001}^{110}$ . To discuss the nature of the coefficient  $b_{prq}^{p'q'r'}$ , we analyze the expression of  $M_{\text{orb}}$  based on the thermal Green function method derived in Ref. [3]:

$$M_{\text{orb}} = \frac{\mu_B}{E_0 N_{\text{uc}} N} \sum_{ab}^{x,y,z} \epsilon_{zab} \times T \sum_{\mathbf{k}, n} \text{ImTr}(\hat{\lambda}_{\mathbf{k}} \hat{G}(k) \hat{v}_{\mathbf{k}}^b \hat{G}(k) \hat{v}_{\mathbf{k}}^c \hat{G}(k)), \quad (\text{S1})$$

where  $\hat{h}_{\mathbf{k}}$  is the tight-binding Hamiltonian with finite  $\boldsymbol{\eta}, \boldsymbol{\phi}$ ,  $\hat{\lambda}_{\mathbf{k}} = \hat{h}_{\mathbf{k}} - \mu \hat{1}$ ,  $v_{\mathbf{k}}^a = \partial \hat{h}_{\mathbf{k}} / \partial k_a$  is the velocity, and  $\hat{G}(k)$  is the Green function.  $\epsilon_{abc}$  is the antisymmetric tensor, and  $k \equiv (\mathbf{k}, \epsilon_n)$  with  $\epsilon_n = (2n+1)\pi T$ . The diagrammatic expression of Eq. [S1] is shown in Fig. S2 (c). The Hamiltonian of the  $4 \times 3$  site model,

$$\hat{h}_{\mathbf{k}} = \hat{h}_{\mathbf{k}}^0 + \hat{\Sigma}_{\mathbf{k}}, \quad (\text{S2})$$

where  $\hat{h}_{\mathbf{k}}^0$  is the  $12 \times 12$  Hamiltonian for  $\boldsymbol{\eta} = \boldsymbol{\phi} = \mathbf{0}$  and  $\hat{\Sigma}_{\mathbf{k}}^{l,m} = \eta_{l,m} f_{\mathbf{k}}^{l,m} + \phi_{l,m} g_{\mathbf{k}}^{l,m}$ , where  $f_{\mathbf{k}}^{l,m}$  [ $g_{\mathbf{k}}^{l,m}$ ] is the form factor of the current order [BO], which is given by the Fourier transform of  $f_{ij}$  [ $g_{ij}$ ] introduced in the main text.  $\eta_{l,m}$  [ $\phi_{l,m}$ ] ( $l, m = 1 \sim 12$ ) is the current order [BO] parameter. Then, the Green function is expanded as

$$\begin{aligned} \hat{G}(k) &= \hat{G}^0(k) + \hat{G}^0(k) \hat{\Sigma}_{\mathbf{k}} \hat{G}^0(k) \\ &+ \hat{G}^0(k) \hat{\Sigma}_{\mathbf{k}} \hat{G}^0(k) \hat{\Sigma}_{\mathbf{k}} \hat{G}^0(k) \\ &+ \dots, \end{aligned} \quad (\text{S3})$$

where  $\hat{G}^0(k) = ((i\epsilon_n - \mu)\hat{1} - \hat{h}_{\mathbf{k}}^0)^{-1}$ . Thus, the coefficient  $m_1$  ( $m_2$ ) can be derived from Eq. [S1], by expanding it with respect to  $\eta_1 \phi_1$  ( $\eta_1 \eta_2 \eta_3$ ) by using Eqs. [S2]-[S3].

Because of the relations

$$h_{\mathbf{k}}^{0,lm} = h_{-\mathbf{k}}^{0,ml}, \quad (\text{S4})$$

$$G^{0,lm}(\mathbf{k}, \epsilon_m) = G^{0,ml}(-\mathbf{k}, \epsilon_m), \quad (\text{S5})$$

$M_{\text{orb}}$  given by Eq. [S1] is zero for  $\boldsymbol{\phi} = \boldsymbol{\eta} = \mathbf{0}$ . Equations [S4] and [S5] are violated for  $\boldsymbol{\eta} \neq \mathbf{0}$  because the current order form factor is odd-parity:  $f_{\mathbf{k}}^{l,m} = -f_{-\mathbf{k}}^{m,l} = -(f_{-\mathbf{k}}^{l,m})^*$ . (Note that  $g_{\mathbf{k}}^{l,m} = f_{-\mathbf{k}}^{m,l} = (g_{-\mathbf{k}}^{l,m})^*$  for the BO. Any Hermitian orders with the wavevector  $\mathbf{q} = \mathbf{0}$  satisfy  $f_{\mathbf{k}}^{l,m} = (f_{\mathbf{k}}^{m,l})^*$ .) Thus, only odd-order terms with respect to  $\boldsymbol{\eta}$  can give nonzero  $M_{\text{orb}}$ .

Here, we consider  $M_{\text{orb}}$  in Eq. [S1] in the original 3-site unit cell picture. Then, the Green function in Eq. [S1] is expressed as  $\hat{G}(k + \mathbf{q}; k) = \hat{G}^0(k) \cdot \delta_{\mathbf{q}, \mathbf{0}} + \sum_m \hat{G}^0(k + \mathbf{q}_m) \hat{\Sigma}_{\mathbf{k}}^{(m)} \hat{G}^0(k) \cdot \delta_{\mathbf{q}, \mathbf{q}_m} + \sum_{m,n} \hat{G}^0(k + \mathbf{q}_m + \mathbf{q}_n) \hat{\Sigma}_{\mathbf{k} + \mathbf{q}_n}^{(m)} \hat{G}^0(k + \mathbf{q}_n) \hat{\Sigma}_{\mathbf{k}}^{(n)} \hat{G}^0(k) \cdot \delta_{\mathbf{q}, \mathbf{q}_m + \mathbf{q}_n} + \dots$ , where  $\hat{G}$  and  $\hat{\Sigma}^{(m)}$  are  $3 \times 3$  matrices. The momentum  $\mathbf{q}_m$  is introduced by  $\hat{\Sigma}_{\mathbf{k}}^{(m)}$ . To obtain finite  $M_{\text{orb}}$ , the total momenta introduced by  $\hat{\Sigma}^{(m_i)}$ ,  $\sum_i^{1,2,\dots} \mathbf{q}_{m_i}$ , should be  $\mathbf{0}$  (modulo original reciprocal vectors).

Hereafter, we discuss the reason for the relation  $m_2 \approx -m_3$ . In this study, the nearest-neighbor order parameters are given in Fig. 1 (c) for the current order and Fig. 1 (a) for the BO. In the original 3-site unit cell picture, the relation  $f_{\mathbf{k}'}^{l'l'} f_{\mathbf{k}}^{l''l''} = -g_{\mathbf{k}'}^{l'l'} g_{\mathbf{k}}^{l''l''}$  ( $\mathbf{k}' = \mathbf{k} + (\mathbf{q}_l - \mathbf{q}_{l'})$ ) holds, where  $l \neq l' \neq l''$ . For instance, we consider a  $m_2$  term given by replacing  $\hat{v}_{x(y)\mathbf{k}}$ ,  $\hat{\lambda}_{\mathbf{k}}$  and  $\hat{G}$  with  $(\partial/\partial k_{x(y)}) \hat{f}_{\mathbf{k}}$ ,  $\hat{f}_{\mathbf{k}}$  and  $\hat{G}^0$ , respectively. The corresponding  $m_3$  term is given by replacing  $(\partial/\partial k_{x(y)}) \hat{f}_{\mathbf{k}}$  with  $(\partial/\partial k_{x(y)}) \hat{g}_{\mathbf{k}}$  in  $m_2$ . Due to the absence of sublattice hybridization around the vHS points [4],  $\hat{G}^0(k)$  is sublattice diagonal around the vHS points, that is,  $G^{0,mm'}(k) = 0$  for  $m \neq m'$ . Then, the relation  $m_2 = -m_3$  is satisfied approximately due to the relation  $f_{\mathbf{k}'}^{l'l'} f_{\mathbf{k}}^{l''l''} = -g_{\mathbf{k}'}^{l'l'} g_{\mathbf{k}}^{l''l''}$  with  $\mathbf{k}' = \mathbf{k} + (\mathbf{q}_l - \mathbf{q}_{l'})$ .

We have just started the analysis based on the Green function method. This is our important future issue.

### C: Analysis of GL free energy with non-analytic $\eta$ -linear term

In the main text, we studied the strong interplay between the bond and current orders under the magnetic field in kagome metals. In Fig. 4, we studied the situation where bond order transition temperature  $T_b^0$  is higher than the chiral current order one  $T_c^0$  at  $h_z = 0$ . We revealed that chiral current order emerges at  $T = T_b^0$  under  $h_z \sim 10^{-4}$  ( $\sim 1\text{T}$ ). That is, the current-order transition temperature is enlarged to  $T_b^0$  under small  $h_z$ , as shown in Fig. 3 (b). The drastic field-induced  $3Q$  current order originates from the non-analytic  $\eta$ -linear terms in  $\Delta \bar{F}$ , that is,  $\Delta \bar{F} = -3h_z [m_1 \boldsymbol{\phi} \cdot \boldsymbol{\eta} + m_3 (\eta_1 \phi_2 \phi_3 + \text{cycl.}) + O(\eta^3)]$ .

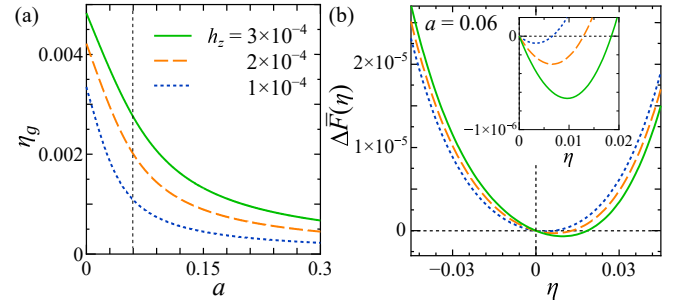


FIG. S3: (a) Induced  $\eta_g$  due to the  $\eta$ -linear term for as a function of  $a$  ( $> 0$ ). Here,  $g = 0.9h_z$  and  $h_z = 1 \sim 3 \times 10^{-4}$ . This result is not sensitive to the choice of  $d$  when  $g$  is small. (b)  $\Delta \bar{F}$  as a function of  $\eta$  for  $a = 0.06$ . (Inset) Enlarged plots around the bottoms.

To understand the effect of the field-induced non-analytic free energy qualitatively, we analyze the following simple GL free energy with a  $\eta$ -linear term:

$$F(\eta) = a\eta^2 + d\eta^4 - g\eta. \quad (\text{S6})$$

Here, we assume  $a$  and  $d$  are positive. When  $g \neq 0$ ,  $F(\eta)$  is minimized at finite  $\eta$  even if  $a > 0$ . The solution is given as

$$\eta_g = X^{1/3}(d^{-1} - 2 \cdot 3^{1/3} a X^{-2/3}) / (2 \cdot 3^{2/3}), \quad (\text{S7})$$

$$X = 9gd^2 + \sqrt{3} \sqrt{d^3(8a^3 + 27dg^2)}. \quad (\text{S8})$$

Note that

$$\eta_g \approx g/2a, \quad (\text{S9})$$

for small  $g$ . Therefore,  $\eta_g$  is finite even when  $a > 0$  due to the  $\eta$ -linear term.

Here, we derive  $d$  and  $g$  from the GL free energy of kagome metal, Eqs. [11] and [10] in the main text. By setting  $\phi = (\phi, \phi, \phi)$  and  $\eta = (\eta, \eta, \eta)$  in Eqs. [11] and [10], we obtain  $d = 6d_i$  and  $g = 3(3m_1\phi + 3m_3\phi^2)h_z$ . When  $d_i = 150$ ,  $m_1 = 5$ ,  $m_3 = 1000$  and  $\phi = 0.01$ , we get  $d = 900$  and  $g = 1.35h_z$ .  $a$  in Eq. [S6] corresponds to  $3a_c$  in the main text. In Fig. 3 (b) in the main text, we set  $a_c = r_c(T - T_c^0)$  with  $r_c = 30$  and  $T_c^0 = 0.005$ , so  $T = T_c^0(2T_c^0 = T_b^0)$  in Fig. 4 (b) corresponds to  $a = 0$  (0.45) in Eq. [S6].

Figure S3 (a) shows  $\eta_g$  given in Eq. [S8] as a function of  $a$ , in the case of  $d = 1000$  and  $g = 1.35h_z$ . We see that  $h_z \sim 10^{-4}$ , which corresponds to  $\sim 1\text{T}$ , induces sizable current order even above  $T_c^0$  if  $a \gtrsim 0$ . The obtained value of  $\eta_g$  in Fig S3 (a) at  $a \approx 0$  is comparable to the field-induced order in Fig. 4 (b). The field-induced  $\eta$  is prominent only when the system at  $h_z = 0$  is close to the current order state (*i.e.*,  $a \gtrsim 0$ ). Asymmetric  $\Delta\bar{F}$  as a function of  $\eta$  is shown in Fig S3 (b).

#### D: Comparison between $\bar{M}_{\text{orb}}$ and $M_{\text{orb}}$

In the main text, we calculated the orbital magnetization  $M_{\text{orb}}$  in kagome metal with current order  $\eta$  and bond-order  $\phi$  using Eq. [3]. Next, we derived its expression up to the third-order of  $\eta$  and  $\phi$ :  $\bar{M}_{\text{orb}} = m_1\phi \cdot \eta + m_2\eta_1\eta_2\eta_3 + m_3(\eta_1\phi_2\phi_3 + \text{cycl.})$ . To obtain the coefficients  $m_1$  and  $m_2$ , we calculate  $M_{\text{orb}}[\eta, \phi]$  very accurately and expand it around  $\eta = \phi = 0$  numerically. For instance, we derive  $m_2$  as  $m_2 = M_{\text{orb}}[(\eta_1, \eta_2, \eta_3), \mathbf{0}] / \eta_1\eta_2\eta_3$  with  $\eta_m = 0.001$ . (Note that  $M_{\text{orb}}[\eta, \mathbf{0}] = 0$  if one of  $\eta_m$  is zero.)

The expression  $\bar{M}_{\text{orb}}$  is very useful to understand the strong interplay between current and bond orders in kagome metal. By considering the field-induced free energy  $\Delta\bar{F} = -3h_z\bar{M}_{\text{orb}}$ , we understand the characteristic phase diagram of kagome metals under the magnetic field.

Here, we verify that  $\bar{M}_{\text{orb}}$  in Eq. [8] well reproduces  $M_{\text{orb}}$  in Eq. [3]. Figures S4 (a)-(c) show the obtained results at  $n = 2.47$  under  $\eta = (\eta, \eta, \eta)/\sqrt{3}$  and  $\phi = (\phi, \phi, \phi)/\sqrt{3}$  as functions of  $\eta$ , in the case of (a)  $\phi = 0$ , (b)

$\phi = +0.01$  and (c)  $\phi = -0.01$ . It is found that  $\bar{M}_{\text{orb}}$  well reproduce the original  $M_{\text{orb}}$  when  $|\eta|, |\phi| \lesssim 0.02$ , unless the shape of the Fermi surface is drastically changed by order parameters.

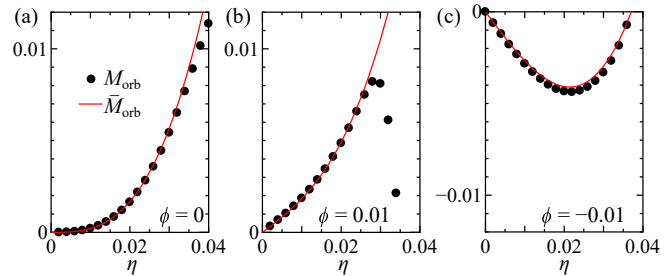


FIG. S4:  $M_{\text{orb}}$  and  $\bar{M}_{\text{orb}}$  for  $\eta = (\eta, \eta, \eta)/\sqrt{3}$  in the cases of (a)  $\phi = \mathbf{0}$  and (b)  $\phi = (\phi, \phi, \phi)/\sqrt{3}$  at  $\phi = +0.01$  and (c)  $-0.01$ .

Next, we examine the validity of the expansion expression  $\bar{M}_{\text{orb}}$  in the realistic 30-orbital model for kagome metal. Figure S5 shows the coefficients  $m_1$  and  $m_2$  given by  $M_{\text{orb}}$  in Eq. [3] in the main text, derived from the region  $|\eta_i|, |\phi_i| < \Lambda$ . The convergence of the obtained results for both  $m_1$  and  $m_2$  is good for  $\Lambda < 0.01$  for wide range of  $n$ , except at the close vicinity of the vHS filling. Therefore, the GL free energy expression [9] in the main text is valid for real kagome metals.

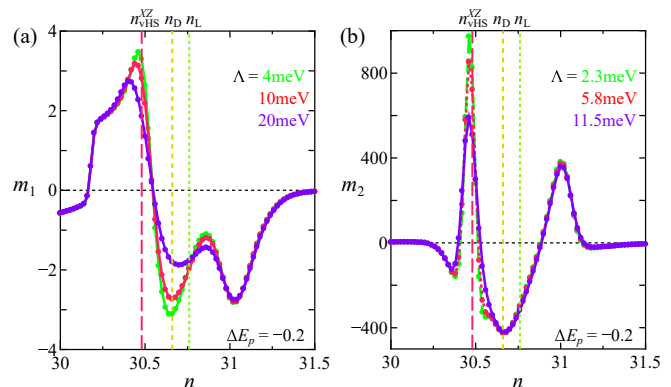


FIG. S5: Obtained coefficients (a)  $m_1$  and (b)  $m_2$  at  $T = 0.005$  derived from the region  $|\eta_i|, |\phi_i| < \Lambda$ .

#### E: $M_{\text{orb}}$ in kagome lattice model with $(t, t') = (-0.5, -0.08)$

In the main text, we studied  $M_{\text{orb}}$  in kagome lattice model with the bare hopping integrals  $t = -0.5$  and  $t' = -0.02$ . The obtained coefficients  $m_1$  and  $m_2$  in  $\bar{M}_{\text{orb}}$  take large values for  $n \approx n_{\text{vHS}}$ , where  $n_{\text{vHS}}$  is the van-Hove filling. Using the obtained coefficients  $m_1$  and  $m_2$ , we discovered the mechanism of the field-induced chiral current order in kagome metals.

To verify the robustness of the obtained results, here we analyze  $M_{\text{orb}}$  in kagome lattice model with large  $t'$ ;  $(t, t') = (-0.5, -0.08)$ . The obtained FS shown in Fig. S6 (a) has large curvature due to large  $|t'|$ . Here, we have introduced the 3Q BO  $\phi = (\phi, \phi, \phi)/\sqrt{3}$  and the 3Q current order  $\eta = (\eta, \eta, \eta)/\sqrt{3}$ . Figure S6 (b) shows the obtained  $M_{\text{orb}}$  [ $\mu_B$ ] per  $V$  atom due to the 3Q current order with  $\phi = 0$ . The relation  $M_{\text{orb}} \propto \eta^3$  is satisfied, and its magnitude is enlarged when  $n \approx n_{\text{vHS}}$ . Figure S6 (c) shows  $M_{\text{orb}}$  [ $\mu_B$ ] due to the coexistence of 3Q current order and 3Q BO. The relation  $M_{\text{orb}} \propto \eta^1$  is satisfied when  $\phi \neq 0$ . Figures S6 (d) and (e) represent the obtained coefficients  $m_1$  and  $m_2$  in  $\bar{M}_{\text{orb}}$ . The magnitudes of  $m_1$  and  $m_2$  for  $t' = -0.08$  are comparable to those for  $t' = -0.02$  given in the main text.

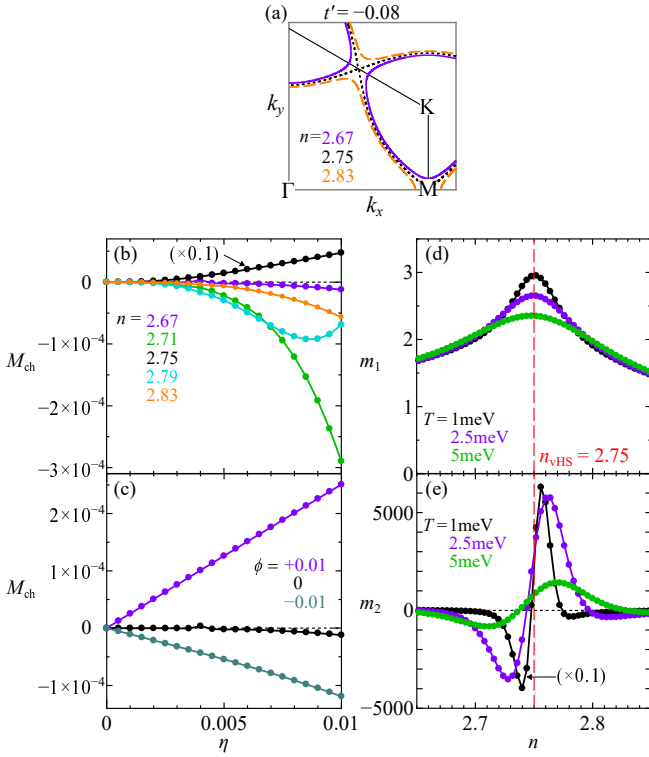


FIG. S6: (a) FS around  $n_{\text{vHS}} = 2.75$  at  $t' = -0.08$ . (b)  $M_{\text{orb}}$  [ $\mu_B$ ] per  $V$  atom due to the 3Q current order  $\eta = (\eta, \eta, \eta)/\sqrt{3}$  at  $T = 1$  meV for  $n = 2.67 \sim 2.83$ . (c)  $M_{\text{orb}}$  due to the coexistence of 3Q current order and 3Q BO at  $n = 2.67$ . Obtained (d)  $m_1$  and (e)  $m_2$  ( $\approx -m_3$ ), per  $V$  atom as a function of  $n$ . Both  $|m_1|$  and  $|m_2|$  are large for  $n \sim n_{\text{vHS}}$ .

### F: Calculation of GL parameters, Renormalization of $a_c$

To verify that the GL free energy coefficients assumed in the main text are qualitatively reasonable, we calculate GL coefficients based on the diagrammatic method. The

4th order GL parameters per unit cell are given as

$$d_1 = I_{1111}^g, \quad (\text{S10})$$

$$d_2 = 2I_{1212}^g + 4I_{1122}^g, \quad (\text{S11})$$

$$d_3 = I_{1111}^f, \quad (\text{S12})$$

$$d_4 = 2I_{1212}^f + 4I_{1122}^f, \quad (\text{S13})$$

where

$$\begin{aligned} I_{hlmn}^w &= \frac{T}{4} \sum_{k, \sigma} \text{Tr} \hat{w}_{\mathbf{q}_h}(k + \mathbf{q}_n + \mathbf{q}_m + \mathbf{q}_l) \\ &\times \hat{G}(k + \mathbf{q}_n + \mathbf{q}_m + \mathbf{q}_l) \\ &\times \hat{w}_{\mathbf{q}_l}(k + \mathbf{q}_n + \mathbf{q}_m) \hat{G}(k + \mathbf{q}_n + \mathbf{q}_m) \\ &\times \hat{w}_{\mathbf{q}_m}(k + \mathbf{q}_n) \hat{G}(k + \mathbf{q}_n) \hat{w}_{\mathbf{q}_n}(k) \hat{G}(k), \end{aligned} \quad (\text{S14})$$

where  $\hat{G}(k)$  is  $3 \times 3$  Green function for the original 3-site kagome lattice model and  $k \equiv (\mathbf{k}, i\epsilon_n)$ . The diagrammatic expression  $I_{hlmn}^w$  is depicted in Fig. S7 (a).  $\hat{w}_{\mathbf{q}}(\mathbf{k})$  is the form factor in the momentum space in the original BZ,  $\hat{f}_{\mathbf{q}}(\mathbf{k})$  or  $\hat{g}_{\mathbf{q}}(\mathbf{k})$ , and  $h, l, m, n$  is 1, 2, or 3. Note that  $f_{\mathbf{q}_m}^{lm}(\mathbf{k})$  [ $f_{\mathbf{q}_m}^{lm}(\mathbf{k})$ ] ( $l, m=1-3$ ) is given by the Fourier transform of  $f_{i,j}^{(m)}$  [ $g_{i,j}^{(m)}$ ] introduced in the main text. The relation  $\mathbf{q}_h + \mathbf{q}_l + \mathbf{q}_m + \mathbf{q}_n = 0$  should be satisfied. Hereafter, we use  $\hat{f}_{\mathbf{q}}(\mathbf{k})$  derived from the density-wave equation in Ref. [5], in which distant-atom components are included. On the other hand,  $\hat{g}_{\mathbf{q}}(\mathbf{k})$  is derived from the nearest-neighbor BO in Fig. 1 (a). In the same way, the analytic expressions of  $d_5$  and  $d_6$  are obtained in Ref. [5].

The obtained numerical results are given in Fig. S7 (b) for  $t' = 0$  and  $t' = -0.02$ . Here, the dimensionless form factors are normalized as  $\max_{\mathbf{k}} |g_{\mathbf{q}_1}^{\text{BA}}(\mathbf{k})| = |g_{\mathbf{q}_1}^{\text{BA}}(\mathbf{k}_A)| = 1$ . (This normalization corresponds to  $|\delta t_{ij}^b| = 1/2$ .) In the same way, we set  $\max_{\mathbf{k}} |f_{\mathbf{q}_1}^{\text{BA}}(\mathbf{k})| = |f_{\mathbf{q}_1}^{\text{BA}}(\mathbf{k}_A)| = 1$ . Thus, the parameter  $d_i = 150$  [ $\text{eV}^{-3}$ ] is consistent with Fig. S7 (b) for  $T \sim 0.01$ . For  $\phi = (\phi, \phi, \phi)$  with  $\phi = 0.01$ , the 4th order term for the BO is  $F_4^{\text{b}} \sim 150 \cdot 6(10^{-2})^4 \sim 10^{-5}$  [eV] for  $d_i = 150$ . The obtained ratios  $r = 2d_1/d_2$  and  $r' = 2d_3/d_4$  are shown in Fig. S7 (c): For  $t' = 0$ , we obtain  $2d_1/d_2 \gg 1$  and  $2d_3/d_4 \gtrsim 1$ . For  $t' = -0.02$ ,  $2d_1/d_2 \sim 1$  and  $2d_3/d_4 \approx 1$ . Both ratios tend to become smaller than unity for larger  $|t'|$ . (Note that  $d_1 \approx d_3 \approx d_5$  and  $d_2 \approx d_4 \approx d_6$  when the form factors satisfy  $f_{ij}^{(m)} = \pm i g_{ij}^{(m)}$ .)

In deriving  $d_1 \sim d_6$  in Fig. S7 (b), we included the self-energy due to the BO fluctuations [5], because the self-energy reduces unrealistic behaviors of  $d_i$  at low temperatures when the inter-sublattice nesting vector is not exactly commensurate [7]. (Note that the present method works well only for  $|t'/t| \ll 1$ .) To calculate the self-energy, we introduce the following effective BO interaction [5]:

$$\hat{H}_{\text{int}} = -\frac{1}{N} \sum_{\mathbf{q}} \frac{v}{2} \hat{O}_{\mathbf{q}}^g \hat{O}_{-\mathbf{q}}^g, \quad (\text{S15})$$

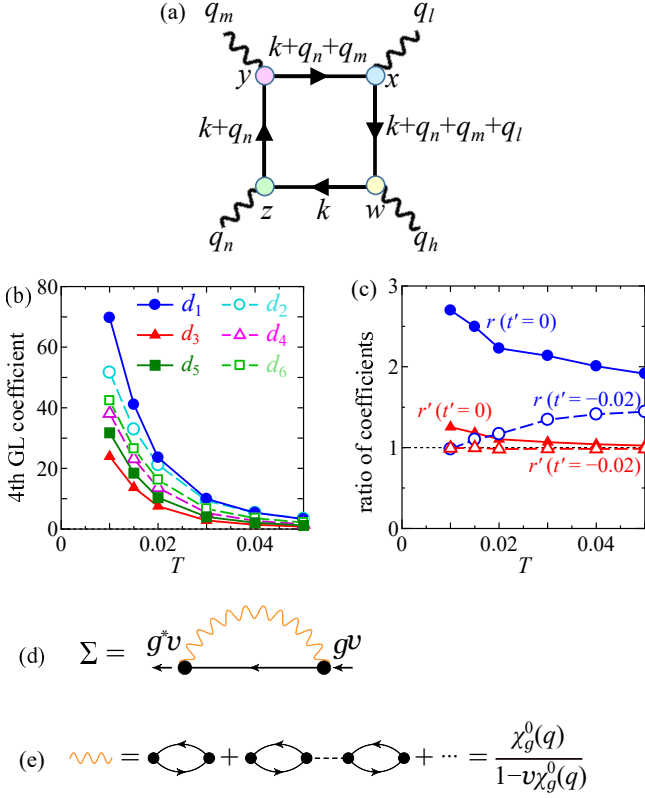


FIG. S7: (a) Diagrammatic expressions of 4th order GL parameters. (b) Numerical results of the 4th order GL parameters as functions of  $T$ . (c) Ratio  $r = 2d_1/d_2$  and  $r' = 2d_3/d_4$  in the case of  $t' = 0$  and  $t' = -0.02$ . (d) Diagrammatic expression of the self-energy driven by the BO fluctuations. (e) Expression of BO susceptibility.

where  $\hat{O}_q^g \equiv \sum_{\mathbf{k}, l, m, \sigma} g_q^{lm}(\mathbf{k}) c_{\mathbf{k}+\mathbf{q}, l, \sigma}^\dagger c_{\mathbf{k}, m, \sigma}$  is the BO operator [6, 8, 9] and  $v$  is the effective interaction. Here, the BO form factor  $g_q^{lm}(\mathbf{k})$  is normalized as  $\max_{\mathbf{k}, l, m} |g_q^{lm}(\mathbf{k})| = 1$  at each  $\mathbf{q}$ , i.e.,  $|\delta t_{ij}^b| \equiv 1/2$  for the nearest sites. We next calculate the on-site self-energy due to BO fluctuations as [5]

$$\Sigma_m(\epsilon_n) = \frac{T}{N^2} \sum_{\mathbf{k}, q, m'', m'''} G_{m'm''}(\mathbf{k} + \mathbf{q}, \epsilon_n + \omega_l) \times B_{mm', mm''}(k, q), \quad (\text{S16})$$

$$B_{ml, m'l'}(k, q) = g_q^{lm}(\mathbf{k})^* g_q^{l'm'}(\mathbf{k}) \cdot v(1 + v\chi_g(q)), \quad (\text{S17})$$

which is shown in Fig. S7 (d). Here, the BO susceptibility  $\chi_g(q)$  is [5]

$$\chi_g(q) = \chi_g^0(q)/(1 - v\chi_g^0(q)), \quad (\text{S18})$$

$$\chi_g^0(q) = \sum_{lm m'l'} \chi_g^{0, lmm'l'}(q), \quad (\text{S19})$$

$$\chi_g^{0, lmm'l'}(\mathbf{q}, \omega_l) = \frac{T}{N} \sum_{\mathbf{k}, \epsilon_n} g_q^{lm}(\mathbf{k})^* G_{lm'}(\mathbf{k} + \mathbf{q}, \epsilon_n + \omega_l) \times G_{l'm}(\mathbf{k}, \epsilon_n) g_q^{m'l'}(\mathbf{k}), \quad (\text{S20})$$

which is shown in Fig. S7 (e). Then, the Green function is given as  $\hat{G}(k) = (i\epsilon_n + \mu - \hat{h}(\mathbf{k}) - \hat{\Sigma}(\epsilon_n))^{-1}$ . The effect of thermal fluctuations described by the self-energy is essential to reproduce the  $T$ -dependence of various physical quantities. In the present numerical study, we calculate Eqs. [S16]-[S20] self-consistently.

We also study the 2nd order GL term, which is derived as  $F_2^b \sim -\chi_g^0(\mathbf{q}_1)R|\phi|^2$  according to Ref. [10]. Here,  $\chi_g^0(\mathbf{q}_1)$  is the irreducible BO susceptibility, and  $R \equiv (d\lambda/dT) \cdot (-T_b^0)$ , where  $\lambda$  is the eigenvalue of the density-wave equation, which is similar to the eigenvalue of the BCS gap equation.  $R \sim O(0.1)$  in usual BO phase transitions [10], while  $R \sim 1$  in BCS superconductivity because of large  $\log T$  singularity of the p-p channel. As a result,  $F_2^b \sim -3 \times 10^{-5}$  [eV] for  $\chi_g^0(\mathbf{q}_1) \sim 3$  and  $R = 0.1$ . Note that  $\chi_g^0(\mathbf{q}_1)R \sim 0.1$  corresponds to  $rT_b^0 \sim 0.1$  in the main text.

Therefore, the BO total free energy is  $F_{\text{tot}}^b \sim -10^{-5}$  [eV] for  $T_b^0 \sim \phi \sim 0.01$  and  $N(0) \sim 1$ . The current-order total free energy  $F_{\text{tot}}^c$  will be comparable to  $F_{\text{tot}}^b$ . Thus, the GL parameters assumed in the main text are qualitatively reasonable. (In BCS superconductors,  $F_{\text{tot}}^c = -\Delta^2 N(0)/2 \sim -10^{-4}$  when  $\Delta = 0.01$  and  $N(0) \sim 1$ .) As discussed in Ref. [10], the specific heat jump  $\Delta C/T$  at the BO or current-order phase transition is much smaller than the BCS value  $\Delta C/T_{\text{SC}} = 1.43N(0)$ .

Finally, we discuss the renormalization of the 2nd order GL coefficient for  $\eta, a_c$ , in the BO phase. Under the  $3Q$  BO phase  $\phi = (\phi, \phi, \phi)/\sqrt{3}$ ,  $a_c$  in Eq. [11] is renormalized as  $\bar{a}_c = a_c + (d_5 + d_6)(2\phi^2/3)$  due to the  $d_5, d_6$  terms. When  $\boldsymbol{\eta} = \mathbf{0}$ , we obtain  $\phi^2 \approx -3a_b/2(d_1 + d_2)$  by neglecting  $b_1$  term, which is allowed except for  $T \approx T_b^0$ . Therefore, we obtain  $\bar{a}_c = \bar{r}_c(T - \bar{T}_c^0)$ , where  $\bar{r}_c = r_c(1 - C)$ ,  $\bar{T}_c^0 = (T_c^0 - CT_b^0)/(1 - C)$ , and  $C \equiv (r_b/r_c)[(d_5 + d_6)/(d_1 + d_2)]$ . Here, we assume  $C < 1$  by referring to the relation  $d_5 + d_6 < d_1 + d_2$  in Fig. S7, owing to the difference between the BO and current order form factors. For detail, see Ref. [35].

### G: $M_{\text{orb}}$ by intra-original-unit-cell current order in kagome lattice

Here, we calculate  $M_{\text{orb}}$  in the case of the intra-original-unit-cell ( $\mathbf{q} = \mathbf{0}$ ) current order in Fig. S8 (a). In this case, the translational symmetry is preserved. The obtained  $M_{\text{orb}}$  is shown in Fig. S8 (b). We find that  $M_{\text{orb}}$  is  $\eta$ -linear even in the absence of the BO, while its coefficient is small for  $n \sim n_{\text{vHS}}$  that is realized in kagome metals. Regardless of the presence of the  $\eta$ -linear term in  $M_{\text{orb}}$ , field-induced intra-original-unit-cell order will be quite small in kagome metals. In fact, the field-induced cLC order at  $\mathbf{q} = \mathbf{0}$  becomes sizable only when its second-order GL coefficient,  $a_c \sim (-1 + \lambda_{\mathbf{q}=\mathbf{0}}^{-1})$ , is very



small. Here,  $\lambda_{\mathbf{q}=\mathbf{0}}$  is the eigenvalue of the current order solution at  $\mathbf{q} = \mathbf{0}$ . However, the relation  $\lambda_{\mathbf{q}=\mathbf{0}} \ll 1$  is obtained in the DW equation analysis in Ref. [5].

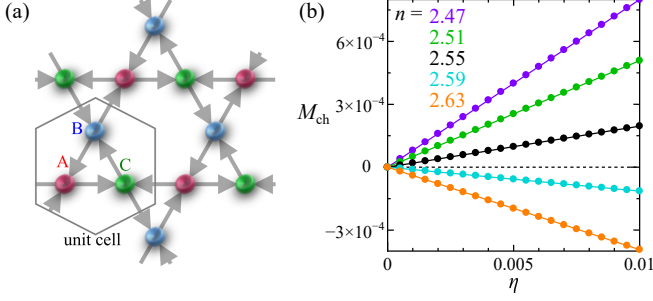


FIG. S8: (a) Intra-original-unit-cell ( $\mathbf{q} = \mathbf{0}$ ) current order. (b)  $M_{\text{orb}}$  for the intra-original-unit-cell current order  $\boldsymbol{\eta} = (\eta, \eta, \eta)/\sqrt{3}$ . We set  $(t, t') = (-0.5, -0.02)$ , and no BO is introduced.

## H: First principles 30-orbital model for kagome metal

In the main text, we analyzed the GL coefficients based on the first-principles 30-orbital model for kagome metals. Figure S9 (a) shows the obtained bandstructure in the  $k_z = 0$  plane. Its FS is shown in Fig. 5 (a). The  $d_{XZ}$ -orbital “pure-type” band corresponds to the present three-orbital model. Its vHS energy is located at  $E_{\text{vHS}}^{XZ} \approx -0.1$ . Also, the  $d_{YZ}$ -orbital forms the “mix-type” band, whose vHS energy is  $E_{\text{vHS}}^{YZ} \approx +0.1$ . In addition, the  $d_{X^2-Y^2} + d_{3Z^2-R^2}$ -orbital forms a pure-type band with the vHS energy  $E_{\text{vHS}}' \approx -0.05$ . Around M point, the  $d_{XZ}$ -orbital band near M point is almost  $k_z$ -independent, while other orbital bands exhibits small  $k_z$ -independences (about  $0.1 \sim 0.2$ ) in the band calculation.

Figure S9 (b) shows the bandstructure with introducing the  $p$ -orbital shift  $\Delta E_p = -0.2$  eV. Its FS is shown in Fig. 5 (b). Here, the  $d_{YZ}$ -orbital (mix-type) band approaches  $E_F$  along the M-M' line, consistently with the APRES measurement in Ref. [11].

Here, we derive the coefficients  $m_1$  and  $m_2$  defined as  $\bar{M}_{\text{orb}} = m_1 \hat{\phi} \cdot \hat{\boldsymbol{\eta}} + m_2 \tilde{\eta}_1 \tilde{\eta}_2 \tilde{\eta}_3$ , where  $\tilde{\eta}_i$  and  $\hat{\phi}_i$  are the order parameter of a specific  $d$ -orbital projected on the conduction band. The results for  $d_{XZ}$ -orbital are shown in Figs. 5 (e)-(h) in the main text. (The weight of  $d_{\Gamma}$ -orbital ( $\Gamma = XZ, YZ$ , etc) on the conduction band is  $W_{XZ} \approx 0.7$ ,  $W_{YZ} \approx 0.3$ ,  $W_{X^2-Y^2} \approx W_{3Z^2-R^2} \approx 0.4$ .) We also calculate  $m_1$  and  $m_2$  when the order parameters emerge on the  $d_{YZ}$ ,  $d_{X^2-Y^2}$ , and  $d_{3Z^2-R^2}$  orbitals. The obtained results are shown in Figs. S9 (a) ( $\Delta E_p = 0$ ) and (b) ( $\Delta E_p = -0.2$ ), as function of the electron filling  $n$ . ( $n = 31$  corresponds to undoped  $\text{CsV}_3\text{Sb}_5$ .) It is found that large  $m_1$  and  $m_2$  are obtained when the current

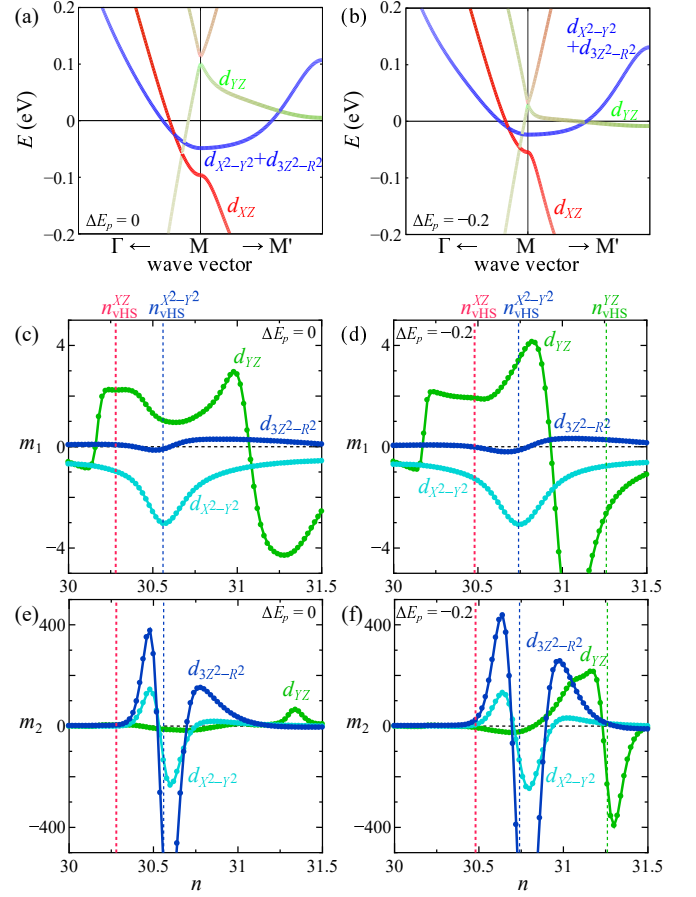


FIG. S9: (a) Bandstructure of  $\text{CsV}_3\text{Sb}_5$  model in the  $k_z = 0$  plane. Its FS is shown in Fig. 5 (a). The  $d_{XZ}$ -orbital band gives the pure-type FS, and the  $d_{YZ}$ -orbital band gives the mix-type FS. The  $d_{X^2-Y^2} + d_{3Z^2-R^2}$ -orbital band gives another pure-type FS.  $\Gamma, M, M'$  are introduced in Fig. 1 (b) in the main text. (b) Bandstructure with the  $p$ -orbital shift  $\Delta E_p = -0.2$  eV. Its FS is shown in Fig. 5 (a). (c)(d) Obtained  $m_1$  for the order parameters in the  $d_{YZ}$ ,  $d_{X^2-Y^2}$ , and  $d_{3Z^2-R^2}$  orbitals for (c)  $\Delta E_p = 0$  model and (d)  $\Delta E_p = -0.2$  model. (e)(f) Obtained  $m_2$  for the order parameters in the  $d_{YZ}$ ,  $d_{X^2-Y^2}$ , and  $d_{3Z^2-R^2}$  orbitals for (e)  $\Delta E_p = 0$  model and (f)  $\Delta E_p = -0.2$  model. In (c)-(f), the vHS filling  $n_{\text{vHS}}^{\Gamma}$  ( $\Gamma = XZ, YZ, X^2-Y^2$ ) is shown. (Note that  $n_{\text{vHS}}^{X^2-Y^2} = n_{\text{vHS}}^{3Z^2-R^2}$ .)

and bond orders emerge on various  $d$ -orbitals. Thus, the present study is valid for various types of current order mechanisms, not restricted to Ref. [5].

## I: Increment of $T_c$ under uniaxial strain in 3Q BO phase

In Ref. [12], it was proposed that  $\text{CsV}_3\text{Sb}_5$  is located at the quantum critical point of the current order ( $T_c^0 \approx 0$  in the absence of the uniaxial strain. The field-induced

( $h_z \sim 9T$ ) current order at  $T_c \sim 20K$  would be explained by the present theory. In addition, Ref. [12] reports the strain induced increment of  $T_c$  in the absence of the magnetic field. It was explained in Ref. [12] based on the GL free energy analysis. Under the uniaxial strain, the degeneracy of the current order transition temperature at  $\mathbf{q} = \mathbf{q}_m$  ( $m = 1 \sim 3$ ),  $T_c^{(m)}$ , is lifted. Then,  $T_c = \max_m T_c^{(m)}$  will be larger than the original  $T_c^0$ .

Here, we present that the strain induced change in the 4th order GL terms causes additional significant contribution to the increment of  $T_c$ . That is, the BO-induced suppression of the current order is drastically reduced by the strain. Considering the  $D_{6h}$  symmetry, we assume that the  $E_{1g}$  symmetry strain ( $\epsilon, \epsilon'$ ) induces the shift of the vHS energy levels as  $\Delta \mathbf{E} \equiv (\Delta E_A, \Delta E_B, \Delta E_C) = \alpha(\epsilon, 0, -\epsilon)$  and  $\Delta \mathbf{E}' \equiv (\Delta E'_A, \Delta E'_B, \Delta E'_C) = (\alpha'/2)(\epsilon', -2\epsilon', \epsilon')$ . Then, the 4th order GL terms are given as

$$\begin{aligned} & \sum_m^{1,2,3} \{d_1^{(m)} \phi_m^4 + d_3^{(m)} \eta_m^4 + 2d_5^{(m)} \phi_m^2 \eta_m^2\} \\ & + \sum_m^{1,2,3} \{d_2^{(o)} \phi_m^2 \phi_n^2 + d_4^{(o)} \eta_m^2 \eta_n^2 + d_6^{(o)} (\phi_m^2 \eta_n^2 + \phi_n^2 \eta_m^2)\}, \end{aligned} \quad (\text{S21})$$

where  $n = m+1$  and  $o = m-1 \pmod{3}$ . When  $\epsilon = \epsilon' = 0$ ,  $d_l^{(m)} = d_l$  for any  $m$  and  $l$ . Below, we show that each  $d_l^{(m)}$  has large  $\epsilon$ - and  $\epsilon'$ -linear terms when  $n \sim n_{\text{vHS}}$ .

Here, we calculate the coefficients  $d_l^{(m)}$  in the three-orbital model based on the Green function methods explained in the SI F. The used model parameters are  $T = 0.01$ ,  $g = 0.6$ ,  $t' = 0$ , and  $\alpha = \alpha' = 1$ . We first study the case of  $n = 2.56$  ( $> n_{\text{vHS}}$ ), whose FS at  $\epsilon' = 0.005$  is shown in Fig. S10 (a). Figure S10 (b) shows the obtained  $d_l^{(m)}$  normalized by its  $\epsilon' = 0$  value, as functions of  $\epsilon'$  for  $|\epsilon'| \leq 0.005$ . We also study the case of  $n = 2.48$  ( $< n_{\text{vHS}}$ ), whose FS at  $\epsilon' = 0.005$  is shown in Fig. S10 (c). Figure S10 (d) shows the normalized  $d_l^{(m)}$  as functions of  $\epsilon'$ . In both cases, the coefficients exhibits sizable  $\epsilon'$ -linear terms, by reflecting the large p-h asymmetry of the kagome lattice model.

In contrast, the irreducible susceptibility with the current form factor  $\chi_{lm,lm}^0(\mathbf{q}) = -T \sum_{\mathbf{k}, n} f_{\mathbf{q}}^{lm}(\mathbf{k})^* G_{ll}(\mathbf{k} + \mathbf{q}, \epsilon_n) G_{mm}(\mathbf{k}, \epsilon_n) f_{\mathbf{q}}^{lm}(\mathbf{k})$  exhibit much smaller relative change in the same range of  $\epsilon'$ ;  $\sim 3\%$  for  $n = 2.56$  and  $\sim 5\%$  for  $n = 2.48$ . The form factor  $f_{\mathbf{q}}(k)$  is introduced in the SI F. (The change in  $\chi_{lm,lm}^0(\mathbf{q}_i)$  modifies the second order coefficient  $a_c$ .) The change in the 3rd order term is very small, which is  $O(\epsilon^2)$  when  $f_{ij}^{(m)} = \pm i g_{ij}^{(m)}$ .

Now, we consider the strain-induced change in the 4th order free energy term. By considering the symmetry property of the Feynman diagrams,  $\Delta F$  due to  $\Delta \mathbf{E} \propto \epsilon$

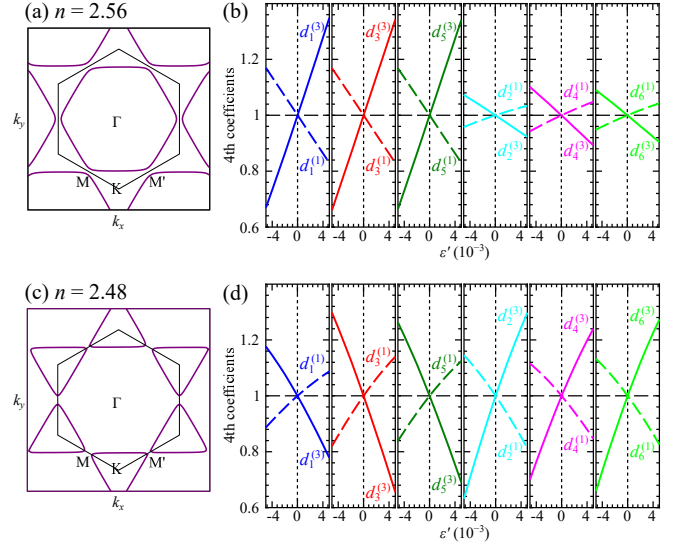


FIG. S10: (a) FS for  $n = 2.56$  with  $\epsilon' = 0.005$  and (b) normalized  $d_l^{(m)}$  ( $m = 1 - 3$ ;  $l = 1 - 6$ ) as functions of the strain  $\epsilon'$  for  $\Delta \mathbf{E}' = \alpha'(\epsilon'/2, -\epsilon', \epsilon'/2)$  with  $\alpha' = 1$ . Their  $\epsilon'$ -linear terms give  $g'_l$  in Eq. [S23]. At  $\epsilon = 0$ ,  $(d_1, d_2, d_3, d_4, d_5, d_6) = (26.09, 62.52, 11.09, 33.97, 14.09, 42.23)$ . (c) FS for  $n = 2.48$  with  $\epsilon' = 0.005$  and (d) obtained  $d_l^{(m)}$  as functions of the strain  $\epsilon'$ . At  $\epsilon' = 0$ ,  $(d_1, d_2, d_3, d_4, d_5, d_6) = (52.40, 19.41, 15.09, 16.60, 21.02, 16.87)$ . In both (b) and (d), the relations  $d_l^{(1)} = d_l^{(2)}$  ( $l = 1 - 6$ ) and  $\partial_{\epsilon'} d_l^{(3)} = -2\partial_{\epsilon'} d_l^{(1)}$  holds. The relation  $\partial_{\epsilon'} d_5^{(m)} \sim -\partial_{\epsilon'} d_6^{(m)}$  means that  $g'_5$  and  $g'_6$  have the same sign. Interestingly,  $\partial_{\epsilon'} d_l^{(m)}$  for  $n > n_{\text{vHS}}$  in (b) and that for  $n < n_{\text{vHS}}$  in (d) have opposite signs. The used parameters are  $T = 0.01$  and  $v = 0.6$ .

is given as

$$\begin{aligned} \Delta F(\epsilon) = & g_1(\phi_1^4 - \phi_2^4) + g_3(\eta_1^4 - \eta_2^4) \\ & + 2g_5(\phi_1^2 \eta_1^2 - \phi_2^2 \eta_2^2) \\ & + g_2(\phi_3^2 \phi_1^2 - \phi_2^2 \phi_3^2) + g_4(\eta_3^4 \eta_1^2 - \eta_2^2 \eta_3^2) \\ & + g_6(\eta_3^4 \phi_1^2 + \eta_1^4 \phi_3^2 - \eta_2^2 \phi_3^2 - \eta_3^2 \phi_2^2), \end{aligned} \quad (\text{S22})$$

where  $g_l$  are  $\epsilon$ -linear.  $g_l$  and  $d_l^{(m)}$  are related as  $\epsilon \cdot (\partial_{\epsilon} d_l^{(1)}, \partial_{\epsilon} d_l^{(2)}, \partial_{\epsilon} d_l^{(3)}) = g_l(1, -1, 0)$  for  $l=\text{odd}$ , and  $= -g_l(1, -1, 0)$  for  $l=\text{even}$ . Also,  $\Delta F'$  due to  $\Delta \mathbf{E}' \propto \epsilon'$  is given as

$$\begin{aligned} \Delta F'(\epsilon') = & g'_1(\phi_1^4 + \phi_2^4 - 2\phi_3^2) + g'_3(\eta_1^4 + \eta_2^4 - 2\eta_3^2) \\ & + 2g'_5(\phi_1^2 \eta_1^2 + \phi_2^2 \eta_2^2 - 2\phi_3^2 \eta_3^2) \\ & + g'_2(\phi_2^2 \phi_3^2 + \phi_3^2 \phi_1^2 - 2\phi_1^2 \phi_2^2) \\ & + g'_4(\eta_2^2 \eta_3^2 + \eta_3^2 \eta_1^2 - 2\eta_1^2 \eta_2^2) \\ & + g'_6(\phi_2^2 \eta_3^2 + \phi_3^2 \eta_2^2 + \phi_3^2 \eta_1^2 + \phi_1^2 \eta_3^2 - 2\phi_1^2 \eta_2^2 - 2\phi_2^2 \eta_1^2), \end{aligned} \quad (\text{S23})$$

where  $g'_l$  are  $\epsilon'$ -linear.  $g'_l$  and  $d_l^{(m)}$  are related as  $\epsilon' \cdot (\partial_{\epsilon'} d_l^{(1)}, \partial_{\epsilon'} d_l^{(2)}, \partial_{\epsilon'} d_l^{(3)}) = g'_l(-1, -1, 2)$  for  $l=\text{odd}$ , and  $= -g'_l(-1, -1, 2)$  for  $l=\text{even}$ .

Here, we consider the possible 3Q BO-current coexisting state motivated by the experiment in Ref. [12]. As explained in Ref. [5], in the case of  $|\phi| \gg |\eta|$  at  $\epsilon = \epsilon' = 0$ , the 3Q BO  $\phi^0 = (\phi^0, \phi^0, \phi^0)/\sqrt{3}$  coexists with the current order  $\eta \propto (\eta_1, \eta_2, -\eta_1 - \eta_2)$  due to the energy gain by the 3rd GL terms with  $b_1 b_2 < 0$ . (The relation  $b_1 b_2 < 0$  is general [5].) Then, the BO-current coexisting state is nematic. Here, we set  $\eta = (\eta, 0, -\eta)/\sqrt{2}$  (or  $\eta = (\eta, -2\eta, \eta)/\sqrt{6}$ ) without loss of generality.

Hereafter, we calculate the change in the current order transition temperature  $\Delta\bar{T}_c(\epsilon)$  ( $\propto \epsilon$ ) under the 3Q BO phase. (Below, we set  $b_1 = -b_2$  for simplicity to obtain the analytic expression.) When  $\eta = \mathbf{0}$ , we obtain the square of the  $i$ -th component of  $\phi$  as  $(\phi_i)^2 = (\phi^0)^2/3 + u_i \psi^2$  ( $u_1 = u_2 = -1$  and  $u_3 = 2$ ), where  $\psi^2 = [(2g_1 + g_2)/(2d_1 - d_2)](\phi^0)^2$  ( $\propto \epsilon$ ). We consider  $|\eta|^2 \sim O(\epsilon)$  by assuming  $T \sim T_c$ . Then, the change in the free energy by  $\Delta\mathbf{E}$  of order  $O(\eta^2)$  is obtained as  $\Delta F = -[(2g_5 + g_6) + D(2g_1 + g_2)]((\phi^0)^2/6) \cdot \eta^2$ , where  $D \equiv (2d_5 - d_6)/(2d_1 - d_2)$ . In the present numerical study,  $D \sim 1$  and  $(2g_5 + g_6) \approx (2g_1 + g_2)$ . (Exactly speaking,  $D = 1.36$  (0.29) for  $n = 2.56$  (2.48).)

In the BO phase at  $\epsilon = 0$ , the original 2nd order GL coefficient  $a_c$  is changed by  $\phi^0 \neq 0$  as

$$\begin{aligned} \bar{a}_c(0) &= a_c + 2(d^5 + d^6)((\phi^0)^2/3) \\ &\propto T - \bar{T}_c(0), \end{aligned} \quad (\text{S24})$$

where  $|\phi^0| \gtrsim T_b$  when  $T \ll T_b$ . For finite  $\epsilon$ , it is changed by  $\Delta F(\epsilon)$  as

$$\begin{aligned} \bar{a}_c(\epsilon) &= \bar{a}_c(0) - [(2g_5 + g_6) + D(2g_1 + g_2)]((\phi^0)^2/6) \\ &\propto T - \bar{T}_c(\epsilon), \end{aligned} \quad (\text{S25})$$

The current order appears in the BO phase when Eq. [S26] becomes negative. Therefore,  $\bar{T}_c$  will increase in proportion to  $\epsilon$  if  $(2g_5 + g_6) > 0$ . (If  $(2g_5 + g_6) < 0$ ,  $T_c$  increases when  $\eta \propto (0, \eta, -\eta)$ .)

In the same way,  $\bar{a}_c(\epsilon)$  is modified by  $\Delta F'(\epsilon')$  as

$$\bar{a}_c(0) - [(2g'_5 + g'_6) + D(2g'_1 + g'_2)]((\phi^0)^2/6). \quad (\text{S26})$$

Note that  $g'_5 = -\epsilon' \partial_{\epsilon'} d_5^{(1)}$  and  $g'_6 = \epsilon' \partial_{\epsilon'} d_6^{(1)}$  has the same sign according to Fig. S10, which is naturally expected analytically.

Considering the drastic  $\epsilon'$ -dependence of  $d_l^{(m)}$  obtained in Fig. S10 (a), in collaboration with the change in  $a_c$  already discussed in Ref. [12], sizable strain-induced increment of the current order transition temperature  $T_c$  reported in Ref. [12] will be realized in the present mechanism.

In the case of  $f_{ij}^{(m)} = \pm i g_{ij}^{(m)}$ ,  $g_l$  and  $g'_l$  coincide with  $l$ =even and  $l$ =odd, respectively. Then,  $D = 1$  and  $(2g_5 + g_6) = (2g_1 + g_2)$ . The main results are valid even in this case.

- 
- [1] D. Ceresoli, T. Thonhauser, D. Vanderbilt, and R. Resta, *Orbital magnetization in crystalline solids: Multi-band insulators, Chern insulators, and metals*, Phys. Rev. B **74**, 024408 (2006).
  - [2] J. Shi, G. Vignale, D. Xiao, and Q. Niu, *Quantum Theory of Orbital Magnetization and Its Generalization to Interacting Systems*, Phys. Rev. Lett. **99**, 197202 (2007).
  - [3] R. Nourafkan, G. Kotliar, and A.-M. S. Tremblay, *Orbital magnetization of correlated electrons with arbitrary band topology*, Phys. Rev. B **90**, 125132 (2014).
  - [4] X. Wu, T. Schwemmer, T. Müller, A. Consiglio, G. Sangiovanni, D. Di Sante, Y. Iqbal, W. Hanke, A. P. Schnyder, M. M. Denner, M. H. Fischer, T. Neupert, and R. Thomale, *Nature of Unconventional Pairing in the Kagome Superconductors AV<sub>3</sub>Sb<sub>5</sub> (A = K, Rb, Cs)*, Phys. Rev. Lett. **127**, 177001 (2021).
  - [5] R. Tazai, Y. Yamakawa, and H. Kontani, *Charge-loop current order and Z<sub>3</sub> nematicity mediated by bond-order Fluctuations in kagome metal AV<sub>3</sub>Sb<sub>5</sub> (A = Cs, Rb, K)*, arXiv:2207.08068 (2022).
  - [6] R. Tazai, Y. Yamakawa, M. Tsuchiizu, and H. Kontani, *d- and p-wave quantum liquid crystal orders in cuprate superconductors,  $\kappa$ -(BEDT-TTF)<sub>2</sub>X, and coupled chain Hubbard models: functional-renormalization-group analysis*, J. Phys. Soc. Jpn. **90**, 111012 (2021).
  - [7] T. Park, M. Ye, and L. Balents, *Electronic instabilities of kagome metals: Saddle points and Landau theory*, Phys. Rev. B **104**, 035142 (2021).
  - [8] H. Kontani, R. Tazai, Y. Yamakawa, and S. Onari, *Unconventional density waves and superconductivities in Fe-based superconductors and other strongly correlated electron systems*, Adv. Phys. **70**, 355 (2021).
  - [9] H. Kontani and S. Onari, *Orbital-Fluctuation-Mediated Superconductivity in Iron Pnictides: Analysis of the Five-Orbital Hubbard-Holstein Model*, Phys. Rev. Lett. **104**, 157001 (2010).
  - [10] R. Tazai, S. Matsubara, Y. Yamakawa, S. Onari, and H. Kontani, *Rigorous formalism for unconventional symmetry breaking in Fermi liquid theory and its application to nematicity in FeSe*, Phys. Rev. B **107**, 035137 (2023).
  - [11] Y. Hu, X. Wu, B. R. Ortiz, S. Ju, X. Han, J. Ma, N. C. Plumb, M. Radovic, R. Thomale, S. D. Wilson, A. P. Schnyder, and M. Shi, *Rich nature of Van Hove singularities in Kagome superconductor CsV<sub>3</sub>Sb<sub>5</sub>*, Nat. Commun. **13**, 2220 (2022).
  - [12] C. Guo, G. Wagner, C. Putzke, D. Chen, K. Wang, L. Zhang, M. G. Amigo, I. Errea, M. G. Vergniory, C. Felser, M. H. Fischer, T. Neupert, and P. J. W. Moll, *Correlated order at the tipping point in the kagome metal CsV<sub>3</sub>Sb<sub>5</sub>*, arXiv:2304.00972.